Geophysical Journal International

Geophys. J. Int. (2026) **245,** 1–22
Advance Access publication 2026 March 26
Research Paper

https://doi.org/10.1093/gji/ggag122

Rapid modelling of borehole induction measurements in layered media along vertical wells using an adaptive Born approximation

D.H. Saputera [1], Carlos Torres-Verdín,[2] M. Jakobsen,[1] K.W.A. van Dongen[3] and N. Jahani[4]

[1]*Department of Earth Science, University of Bergen, 5020,Bergen, Norway. E-mail: durra.saputera@uib.no, durra.handri@gmail.com*
[2]*Hildebrand Department of Petroleum and Geosystems Engineering, The University of Texas at Austin, 78712,Austin, TX, USA*
[3]*Department of Imaging Physics, Delft University of Technology, 2628 CJ,Delft, the Netherlands*
[4]*NORCE Norwegian Research Centre, 5008,Bergen, Norway*

Accepted 2026 March 17. Received 2026 February 24; in original form 2025 August 5

SUMMARY

The Born approximation offers a computationally efficient alternative to full electromagnetic (EM) forward modelling, but suffers from limited accuracy due to its reliance on a fixed background conductivity. In this work, we develop an *adaptive Born approximation* that treats the background medium as a tunable parameter to enhance accuracy in a goal-oriented manner. The background conductivity is selected locally for each measurement configuration using spatial sensitivity functions, enabling accurate modelling in both isotropic and anisotropic media. In this study, we primarily focus on horizontally layered earth models penetrated by a vertical well to investigate the fundamental behaviour of the approximation in a simplified setting. We formulate our approach to be applicable to general anisotropic media by using the Green's function defined for a homogeneous medium. Furthermore, the approach extends to cases where the background conductivity is isotropic while the actual medium is anisotropic. For a layered medium, the orientation of induced current densities relative to the layering provides physical intuition for background selection, drawing analogies to Voigt- and Reuss-type bounds. While these analogies offer useful guidance, our numerical results do not always conform to the expectations derived from them. Among the averaging schemes evaluated, arithmetic averaging generally yields the most accurate results. Numerical experiments indicate that the adaptive approach significantly outperforms fixed-background models across a range of frequencies, spacings and conductivity contrasts. Furthermore, an example with a 3-D structure illustrates the method's broader applicability beyond the horizontally layered earth setting. This framework provides a principled and efficient path toward fast, accurate EM borehole modelling for real-time well geosteering and subsurface electrical imaging.

Key words: Electromagnetic theory; Numerical approximations and analysis; Numerical modelling.

1 INTRODUCTION

Tri-axial deep-sensing borehole electromagnetic (EM) induction measurements play a critical role in real-time well geosteering by providing high-resolution insights into the electrical conductivity of formations surrounding the borehole. These measurements enable precise characterization of nearby geological structures and their saturating fluids near the borehole. Depending on the surrounding electrical conductivity and tool configuration, it can provide tens of metres of depth of investigation, thereby supporting informed, real-time drilling decisions (G. Wilson *et al.* 2019; N. Clegg *et al.* 2022).

Accurate imaging of spatially heterogeneous and anisotropic subsurface environments often necessitates 3-D inversion. While recent studies have shown progress toward real-time 3-D inversion (N. Clegg *et al.* 2022; A. Elkhamry *et al.* 2023), the process remains computationally intensive, largely due to the high computational cost associated with forward modelling. This challenge motivates the development of fast yet accurate forward modelling techniques.

Among the numerical methods used to simulate borehole EM responses, such as finite-difference (S. Davydycheva *et al.* 2003; J. Hou *et al.* 2006) and finite-element methods (D. Pardo *et al.* 2021), the integral equation (IE) method offers a distinct advantage: it requires discretization only in spatial regions that deviate from a known background medium. Within this framework, several scattering approximations have been proposed, including the Born approximation, extended Born approximation and single-spherical scattering model (T.M. Habashy *et al.* 1993).

The choice of background conductivity is a key aspect of the IE method, given that the error and convergence of linear approximations are typically proportional to the contrast between the actual and the background medium (T.M. Habashy *et al.* 1993; G. Hursan

& M.S. Zhdanov 2002). Consequently, the background conductivity becomes a tunable parameter that can be adaptively selected to improve the accuracy of the approximation as the locations of transmitter and receiver are varied in relation to the scattering target, as well as the operating frequency. For instance, N.B. Christensen (1997) introduced an adaptive background based on spatial sensitivity functions derived from the Born approximation in time-domain EM imaging. B. S. Singer *et al.* (2003) recommended selecting the background based on extrema of the conductivity distribution, while S. Bensdorp *et al.* (2014) suggested dynamic updates during inversion.

In this work, we focus on the adaptive Born approximation and develop an adaptive scheme for rapid simulation of borehole EM measurements. The kernel of the integral formulation of Maxwell's equations can be thought of as a space-weighting operator of the conductivity distribution between both transmitter and receiver (C. Torres-Verdin & T.M. Habashy 1994; N.B. Christensen 1997). Under the Born approximation, this kernel becomes a linear operator, indicating a weighted summation of the conductivity contrast that depends on the transmitter–receiver geometry, frequency and background conductivity. This means that each measurement configuration samples the medium differently, thereby invoking the thought of using a background conductivity that reflects the contributions of different media in the sensitive region.

By interpreting the integral kernel in the Born approximation as a spatial sensitivity function, we can identify the region where the measurement is most responsive to changes in conductivity. This insight allows us to define the background conductivity through a weighted averaging process, using the kernel itself as the weighting function. The result is an adaptive Born approximation, in which the background conductivity reflects the contributions of the surrounding medium rather than being fixed *a priori*. By tailoring the background conductivity to each configuration, the adaptive Born approximation improves the fidelity of the approximation while preserving its computational efficiency. This approach is inspired by effective medium theory, where the appropriate averaging scheme depends on the orientation of the induced current density relative to the layering. For example, Voigt-type (arithmetic) and Reuss-type (harmonic) bounds correspond to current flow parallel and normal to the layers, respectively (S. Moskow *et al.* 1999; S. Davydycheva *et al.* 2003; T. Habashy & A. Abubakar 2007).

To compute the spatial sensitivity function, we focus on the usage of a Green's function for a homogeneous medium, which can be computed with simple expressions for a 3-D spatial domain. A key advantage of the Born approximation with this Green's function is that it reduces the forward modelling problem to numerical integration of the Green's tensor, which depends on the source–receiver configuration, frequency and background conductivity. This aligns with our objective of developing a goal-oriented modelling, which seeks to optimize accuracy at specific observation points for a given source configuration. While goal-oriented strategies are typically associated with finite element methods, that is, goal-oriented adaptive grid refinement (K. Key & J. Ovall 2011; Z. Ren *et al.* 2013), we show that similar principles can enhance the performance of linear approximations—such as the Born model—within the integral equation framework.

We focus the numerical experiments in this study on the case of EM induction measurements across a horizontally layered medium, where the electric fields are either parallel or orthogonal to layer interfaces. This configuration is chosen for several reasons: First, we have access to a semi-analytical solution (M. Shahriari *et al.* 2018) that allows for fast and accurate computation without concerns related to numerical discretization. Secondly, in the vertical well setting, the conductivity tensor and magnetic field components are aligned with the principal coordinate axes, hence eliminating the need to account for cross-component interactions or tensor projections. In such media, certain source–receiver configurations induce current densities that are predominantly parallel or normal to layering, allowing for intuitive physical interpretations. Building on this condition, we further extend the adaptive approach to support general anisotropic conductivity distributions.

Although analogies to effective medium theory provide useful physical intuition, our numerical results do not always align with expectations derived from these bounds. Nevertheless, the adaptive strategy proves effective in practice, particularly in layered and anisotropic media where fixed-background models entail some technical difficulties. This strategy underscores the value of treating the background as a configuration-dependent parameter, selected to improve accuracy at receiver locations.

Throughout this study, we assume that borehole EM measurements operate in the diffusion regime of Maxwell's equations, where displacement currents are negligible. Consequently, the proposed method may be less effective in wave-dominated regimes.

The remainder of this paper is organized as follows: Section 2 presents the theoretical formulation of the adaptive Born approximation. Section 3 describes the numerical experiments and evaluates the performance of the proposed method. We begin with simulations in a horizontally layered model, benchmarked against a semi-analytical solution. A 3-D example is also included to verify the applicability of the method to more general structures. Section 4 provides an analysis of the results presented in Section 3. Finally, Section 5 concludes the paper with a summary of key findings and outlines directions for future research.

2 THEORY

2.1 Integral equation method

The theory for modelling EM measurements acquired in wells is governed by Maxwell's equations for heterogeneous media in the frequency domain, namely (G.W. Hohmann 1983; D.B. Avdeev *et al.* 2002),

$$\nabla \times \mathbf{E}(\mathbf{x}, \omega) = i\omega\mu \mathbf{H}(\mathbf{x}, \omega) + \mathbf{J}^H(\mathbf{x}, \omega), \tag{1}$$
$$\nabla \times \mathbf{H}(\mathbf{x}, \omega) = \widehat{\boldsymbol{\sigma}}(\mathbf{x}, \omega)\mathbf{E}(\mathbf{x}, \omega), \tag{2}$$

where $\mathbf{E}(\mathbf{x}, \omega)$ and $\mathbf{H}(\mathbf{x}), \omega)$ denote the total electric and magnetic fields, respectively. $\mathbf{J}^H(\mathbf{x}, \omega)$ denotes the magnetic source term, ω is angular frequency, $\mathbf{x}$ is the position vector in 3-D space $\mathbb{R}^3$ and μ is magnetic permeability. $\widehat{\boldsymbol{\sigma}}(\mathbf{x}, \omega) = \boldsymbol{\sigma}(\mathbf{x}) - i\omega\boldsymbol{\varepsilon}(\mathbf{x})$ is the complex-valued electric conductivity, where $\boldsymbol{\sigma}(\mathbf{x})$ and $\boldsymbol{\varepsilon}(\mathbf{x})$ are the frequency-independent electric conductivity and dielectric permittivity, respectively, with $i = \sqrt{-1}$ the imaginary unit. We assume a constant magnetic permeability equal to the magnetic permeability of vacuum μ_0. Additionally, we consider that the borehole instruments operate in the diffusion regime (i.e. quasi-static approximation), where the contribution of dielectric permittivity in the imaginary part of the complex-valued conductivity becomes negligible and we set $\widehat{\boldsymbol{\sigma}}(\mathbf{x}, \omega) = \boldsymbol{\sigma}(\mathbf{x})$.

By decomposing the total electric and magnetic fields in Maxwell's equations into background and scattered fields, they can be expressed using the following integral equations (G.W. Hohmann 1983):

$$\mathbf{E}(\mathbf{x}, \omega) = \mathbf{E}^{(0)}(\mathbf{x}, \omega) + \int_\Omega \mathbf{G}^{(0,EE)}(\mathbf{x}, \mathbf{x}', \omega)\, \Delta\boldsymbol{\sigma}(\mathbf{x}')\, \mathbf{E}(\mathbf{x}', \omega)\, \mathrm{dV}(\mathbf{x}'), \tag{3}$$
$$\mathbf{H}(\mathbf{x}, \omega) = \mathbf{H}^{(0)}(\mathbf{x}, \omega) + \int_\Omega \mathbf{G}^{(0,HE)}(\mathbf{x}, \mathbf{x}', \omega)\, \Delta\boldsymbol{\sigma}(\mathbf{x}')\, \mathbf{E}(\mathbf{x}', \omega)\, \mathrm{dV}(\mathbf{x}'). \tag{4}$$

The first and second terms on the right-hand side of eqs (3) and (4) designate the background and scattered fields, respectively. The symbol $\mathbf{G}$ denotes the dyadic Green's tensor, where the superscript (0) refers to the fields and Green's tensor defined for a homogeneous background medium with electrical conductivity $\boldsymbol{\sigma}^{(0)}$. The letters EE and HE in the superscript of the Green's tensor specify the resulting electric and magnetic fields, respectively, due to an electric source. The domain Ω is defined in the 3-D space $\mathbb{R}^3$, and the conductivity contrast is given by $\Delta\boldsymbol{\sigma}(\mathbf{x}) = \boldsymbol{\sigma}(\mathbf{x}) - \boldsymbol{\sigma}^{(0)}$, where $\boldsymbol{\sigma}(\mathbf{x})$ denotes the actual (possibly anisotropic) medium conductivity. Additional details regarding the expression for the Green's tensor are provided in the Appendix. Assuming that the source of EM excitation is a point-source magnetic dipole, that is,

$$\mathbf{J}^H(\mathbf{x}, \omega) = i\omega\mu_0\, \delta(\mathbf{x} - \mathbf{x_s})\, \mathbf{m}, \tag{5}$$

with $\mathbf{m}$ the source orientation vector and $\mathbf{x}_s$ the source location, one can express the background fields as follows:

$$\mathbf{E}^{(0)}(\mathbf{x}, \mathbf{x}_s, \omega, \mathbf{m}) = \mathbf{G}^{(0,EH)}(\mathbf{x}, \mathbf{x}_s, \omega)\ \mathbf{m}, \tag{6}$$
$$\mathbf{H}^{(0)}(\mathbf{x}, \mathbf{x}_s, \omega, \mathbf{m}) = \mathbf{G}^{(0,HH)}(\mathbf{x}, \mathbf{x}_s, \omega)\ \mathbf{m}. \tag{7}$$

A numerical solution of the convolution integral in eqs (3) and (4) can be obtained using the method of moments and by discretizing the subsurface distribution of electrical conductivity around the borehole EM source/receiver into a set of cubic grid blocks (W.C. Gibson 2021). For discretization with cubic grid blocks, integrating the Green's tensor of a grid block over a spherical domain with an equivalent volume is one of the methods used to calculate the contribution of the singularity of the Green's tensor (P. Zwamborn & P.M. van den Berg 1992; G. Gao *et al.* 2005; M. Jakobsen & S. Tveit 2018).

The discretization of eq. (3) leads to a linear system which can be solved to obtain the total electric field $\mathbf{E}(\mathbf{x}, \omega)$. This can be solved efficiently with a matrix-free implementation using a Krylov subspace. Furthermore, fast Fourier transforms (FFT) can be used to compute the convolution integral operator and pre-conditioners can be implemented to reduce the computation time (G. Hursan & M.S. Zhdanov 2002; S. Fang *et al.* 2006; D. H. Saputera *et al.* 2024). Afterward, the computation of the total magnetic field is performed by direct numerical integration in eq. (4).

2.2 Adaptive Born approximation

To aid the clarity of the derivations involving the Born approximation, we first introduce the notation and tensor representation adopted in this study. Because the magnetic fields of the tri-axial borehole induction measurement are often expressed as a tensor component H_{rs}, we will write the fields, Green's function and the conductivity tensor in the formula using the Einstein summation convention. We use the convention where r indicates the magnetic field component at the receiver position, whereas s corresponds to the non-zero component of the source vector, indicating its orientation. Typically, the tool consists of three co-located receivers and three co-located transmitter coils oriented in orthogonal directions. In a vertical well, indices r and s directly indicate the direction of horizontal (x and y) and vertical (z) principal axes, respectively.

Additionally, when dealing with the formulation involving anisotropic media, it is convenient to decompose the conductivity tensor into its tensorial and scalar components, namely, (M. Jakobsen *et al.* 2023; D.H. Saputera *et al.* 2025):$\sigma_{ij} = \sum_p C_{ij}^{(p)} \sigma^{(p)}$,where $C_{ij}^{(p)}$ are the elements of the 3×3 basis tensor for the p^{th} component of the 3×3 conductivity tensor σ_{ij}, with subscripts i and j designating the row and column index of a tensor, respectively. The same form can also be applied to the background conductivity when it is also anisotropic. For example, we consider the case of a medium that exhibits vertical transverse isotropy (VTI) in this section. We can

decompose the conductivity of a VTI medium into its horizontal and vertical conductivity with the following basis tensors:

$$C_{ij}^{(1)} = \begin{bmatrix} 1 & 0 & 0 \\ 0 & 1 & 0 \\ 0 & 0 & 0 \end{bmatrix}, \text{and } C_{ij}^{(2)} = \begin{bmatrix} 0 & 0 & 0 \\ 0 & 0 & 0 \\ 0 & 0 & 1 \end{bmatrix}, \tag{8}$$

where the upper-scripts (1) and (2) identify the horizontal and vertical conductivity, respectively.

The Born approximation assumes that the higher order scattered fields are negligible and the total electric field $E_{ks}(\mathbf{x}, \omega)$ on the right-hand side of eq. (3) is approximated by the background field $E_{ks}^{(0)}(\mathbf{x}, \omega)$. Here, the first subscript indicates the k^{th} component of the field, and the addition of the second subscript denotes the dependency of the fields in eq. (3) on the s-th source orientation. Using the conductivity tensor definition in eq. (8), the approximation of the total magnetic field for all tri-axial components at the receiver position $\mathbf{x}_r$ is expressed as

$$H_{rs}\left(\mathbf{x}_r, \mathbf{x}_s, \omega\right) \approx H_{rs}^{(0)}\left(\mathbf{x}_r, \mathbf{x}_s, \omega\right) + \sum_p \int_\Omega G_{ri}^{(0,HE)}\left(\mathbf{x}_r, \mathbf{x}', \omega\right) C_{ij}^{(p)} \Delta\sigma^{(p)}\left(\mathbf{x}'\right)\, E_{js}^{(0)}\left(\mathbf{x}', \mathbf{x}_s, \omega\right) \mathrm{dV}(\mathbf{x}'), \tag{10}$$

$$\Delta\sigma^{(p)}(\mathbf{x}) = \sigma^{(p)}(\mathbf{x}) - \sigma^{(0,p)}, \tag{11}$$

where $\Delta\sigma^{(p)}(\mathbf{x})$ is the conductivity contrast between the p^{th} component of the actual ($\sigma^{(p)}(\mathbf{x})$) and a constant background ($\sigma^{(0,p)}$) conductivity. Since the Born approximation assumes weak scattering, its accuracy depends on the difference between the background and actual conductivity (T.M. Habashy *et al.* 1993). Consequently, the choice of background conductivity becomes critical, and this point is discussed in the next subsections.

2.2.1 Adaptive background conductivity for anisotropic media

We rearrange the second term on the right-hand side of eq. (10) to define the scattered magnetic field, $H_{rs}^{(s)}\left(\mathbf{x}_r, \mathbf{x}_s, \omega\right)$, as

$$H_{rs}^{(s)}\left(\mathbf{x}_r, \mathbf{x}_s, \omega\right) = \sum_p \int_\Omega K_{rs}^{(0,p)}\left(\mathbf{x}_r, \mathbf{x}_s, \omega, \mathbf{x}'\right) \Delta\sigma^{(p)}\left(\mathbf{x}'\right) \mathrm{dV}(\mathbf{x}'), \tag{12}$$

where the kernel $K_{rs}^{(0,p)}\left(\mathbf{x}_r, \mathbf{x}_s, \omega, \mathbf{x}'\right)$ is defined as

$$K_{rs}^{(0,p)}\left(\mathbf{x}_r, \mathbf{x}_s, \omega, \mathbf{x}'\right) = G_{ri}^{(0,HE)}\left(\mathbf{x}_r, \mathbf{x}', \omega\right)\, C_{ij}^{(p)} E_{js}^{(0)}\left(\mathbf{x}', \mathbf{x}_s, \omega\right). \tag{13}$$

From eq. (12), we directly observe that the scattered field is a weighted integral of the conductivity contrast components. This space-weighting function depends on the magnetic field components, source–receiver spacing and frequency, as can be observed from eq. (13). Additionally, because both the Green's function and the background electric fields depend on the choice of the background conductivity, the space-weighting kernel also depends on it. This kernel is none other than the sensitivity function or the Fréchet derivative of the total magnetic field $H_{rs}\left(\mathbf{x}_r, \mathbf{x}_s, \omega\right)$ with respect to the p^{th} component of the conductivity tensor $\sigma^{(p)}\left(\mathbf{x}\right)$.

Based on the above, we propose choosing a background conductivity based on a weighted averaging of the conductivity around the transmitter and receiver to improve the accuracy of the approximation. In situations where the background and actual conductivity of the medium have the same type of anisotropy, the weighted averaging for each background conductivity component may be taken as

$$\sigma^{(0,p)} = \int_\Omega \bar{w}\left(\mathbf{x}, \sigma^{(0,p)}\right) \sigma^{(p)}(\mathbf{x}) \mathrm{dV}(\mathbf{x}), \tag{14}$$

where $\bar{w}$ is a normalized weight quantity written as

$$\bar{w}\left(\mathbf{x}, \sigma^{(0)}\right) = \frac{w\left(\mathbf{x}, \sigma^{(0)}\right)}{\int_\Omega w\left(\mathbf{x}, \sigma^{(0)}\right) \mathrm{dV}(\mathbf{x})}. \tag{15}$$

The weight is chosen as the absolute value of the sensitivity function of the magnetic field component H_{rs} with respect to the p^{th} conductivity tensor component for a given source and receiver configuration, which is the kernel $K_{rs}^{(0,p)}$ defined in eq. (13). Hence, the chosen weight equals

$$w\left(\mathbf{x}, \sigma^{(0,p)}\right) = \left|K_{rs}^{(0,p)}\left(\mathbf{x}_r, \mathbf{x}_s, \omega, \mathbf{x}\right)\right|. \tag{16}$$

Given the fact that different magnetic field components and measurement configurations have different spatial sensitivity kernels, we adapt the background conductivity by considering the (a) frequency, (b) transmitter–receiver location, (c) transmitter orientation and (d) vector component of the measured magnetic field. Accordingly, the conductivity contrast is now defined as

$$\Delta\sigma^{(p)}\left(\boldsymbol{\gamma}, \mathbf{x}\right) = \sigma^{(p)}(\mathbf{x}) - \sigma^{(0,p)}(\boldsymbol{\gamma}), \tag{17}$$

where the configuration-dependent parameter vector is given by $\boldsymbol{\gamma} := [\omega, \mathbf{x}_r, \mathbf{x}_s, r, s]$. As a result, the Born approximation in eq. (10) becomes adaptive to different components and measurement configurations. This adaptiveness is goal-oriented, with the goal to account for implicit, configuration-dependent averaging that arises from the self-consistent dependence of the sensitivity on the background conductivity, as shown in eq. (14).

The implicit average in eq. (14) can be computed through an iterative averaging procedure, repeated until convergence is achieved, for example, the difference between the left- and right-hand side of eq. (14) is less than 0.1 per cent. Alternatively, a nonlinear solver can be used to find the optimum value that satisfies (14) in the case of divergence. The process begins with an initial background conductivity at the first position—for example, 1 S m^{-1}—and the resulting value subsequently serves to initialize the iterative process at the next position.

By using the absolute value of the sensitivity function, we avoid a negative- or complex-valued background conductivity in the averaging result and stabilize the process by keeping the conductivity within the range of actual conductivity values. To explore different possibilities, we present different averaging schemes based on eq. (14), where the kernel is allowed to be a complex-valued function, both with and without the real and positivity constraints on the background conductivity.

In the case where a certain measurement configuration is not sensitive to a conductivity tensor component, indicated by zero in the normalization factor, the conductivity of this component is set to be equal to the conductivity component with non-zero sensitivity. This approach is, in principle, applicable for general anisotropic media by adapting the basis tensor to different types of anisotropy.

One limitation of the new approach is that the spatial domain needs to be discretized everywhere. This is because the background conductivity will be a weighted spatial average of the distribution of electrical conductivity, instead of a specifically designated value.

2.2.2 Adapting isotropic background conductivity to anisotropic media

The approach presented in the previous section works whenever the degree of anisotropy of the actual medium is the same as the background conductivity used to compute the Green's function. However, one may use the isotropic Green's function to provide a different internal electric field approximation since it has a simpler form to be implemented numerically. For clarity, the isotropic background can be written in the form (8) as$\sigma_{ij}^{(0)} = I_{ij}\,\sigma^{(0)}$,where I_{ij} are the elements of a 3×3 identity tensor. Assuming an isotropic background conductivity, the scattered field in anisotropic media, where the actual conductivity tensor has zero off-diagonal components, can be expressed as

$$H_{rs}^{(s)}(\mathbf{x}_r, \mathbf{x}_s, \omega) = \sum_p \int_\Omega K_{rs}^{(0,p)}(\mathbf{x}_r, \mathbf{x}_s, \omega, \mathbf{x}')\,\left[\sigma^{(p)}(\mathbf{x}') - \sigma^{(0)}\right] \mathrm{dV}(\mathbf{x}'). \tag{18}$$

We observe that the scalar factor of the isotropic background conductivity $\sigma^{(0)}$ appears on the weighted integral of every conductivity component. Considering this, we propose adapting the isotropic background conductivity for each magnetic field component and source–receiver configuration using the following weighted-average:

$$\sigma^{(0)}(\boldsymbol{\gamma}) = \sum_p \int_\Omega \bar{w}^{(p)}\left[\mathbf{x}, \sigma^{(0)}(\boldsymbol{\gamma})\right] \sigma^{(p)}(\mathbf{x}) \mathrm{dV}(\mathbf{x}), \tag{20}$$

and the normalization factor $\bar{w}$ is chosen as

$$\bar{w}^{(p)}\left[\mathbf{x}, \sigma^{(0)}(\boldsymbol{\gamma})\right] = \frac{w^{(p)}\left[\mathbf{x}, \sigma^{(0)}(\boldsymbol{\gamma})\right]}{\sum_p \int_\Omega w^{(p)}\left[\mathbf{x}, \sigma^{(0)}(\boldsymbol{\gamma})\right] \mathrm{dV}(\mathbf{x})}, \tag{21}$$

with the weight chosen as the absolute value of the sensitivity function of the magnetic field with respect to the p^{th} component of the conductivity tensor for a given source–receiver configuration defined in eq. (13). The key idea is that the isotropic conductivity is now averaged not only spatially, but also across the conductivity tensor components by incorporating different sensitivity kernels with respect to each component.

3 NUMERICAL RESULTS

In this section, we present numerical experiment results to verify and benchmark the accuracy of the adaptive Born approximation. For benchmarking purposes, results are compared against an existing 1.5-D semi-analytical solution (M. Shahriari *et al.* 2018). All numerical experiments described in this study are performed on a laptop with an AMD Ryzen 7 4800H processor and NVIDIA GeForce RTX 3060 Laptop GPU using MATLAB with GPU support enabled.

The numerical experiments in this study focus mainly on the vertical borehole case to first examine the fundamental behaviour of the adaptive Born approximation in a simplified setting. We simulate borehole-logging conditions with varying parameters across a three-layered medium in a vertical well, as described in Fig. 1. The top of the middle (sandwiched) layer is located at $z = 45.72$ m and it has a thickness of 15.24 m. The conductivity values for each layer are specified in the corresponding subsections. All data are plotted at the midpoint between the source and receiver locations, from $z = 0$ to 121.94 m in 1.524 m intervals. The tri-axial logging tool configurations used in this study are inspired by existing commercial deep-sensing borehole EM tools that operate between 2 and 96 kHz, with receiver spacings ranging from approximately 7 to 30 m behind the transmitter (e.g. see F. Antonsen *et al.* 2022). Finally, a simulation of the adaptive Born approximation on a 3-D model is presented in the last subsection to assess its applicability in a more realistic setting.

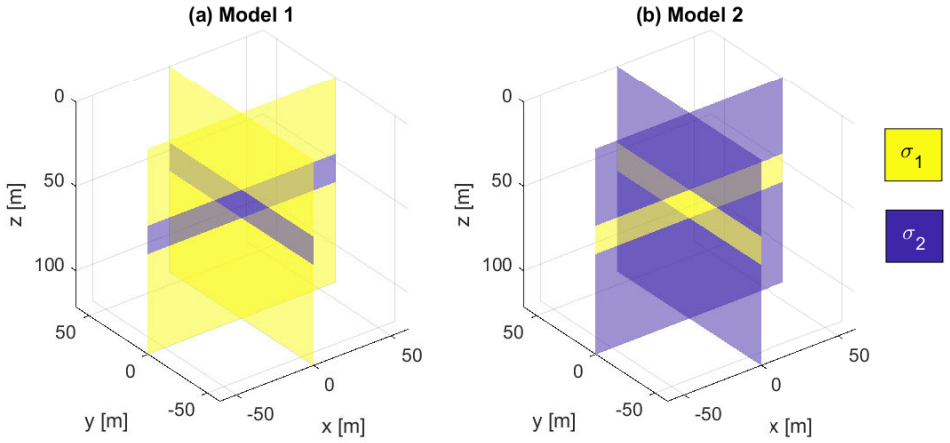

Figure 1. Model 1 (left): Conductive layer bounded by resistive layers. Model 2 (right): Resistive layer in the middle. The same colour indicates an equal conductivity value.

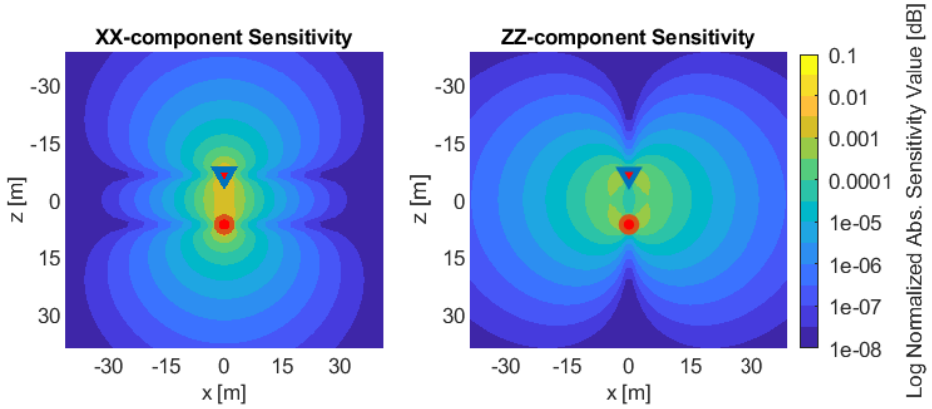

Figure 2. Normalized absolute value of the sensitivity functions for H_{xx} and H_{zz} measurement configurations in the xz-plane of a simulation window. The background conductivity is set to 1/30 S m^{-1}. The dots and triangles identify the transmitter and receiver, respectively.

The iteration process of the adaptive Born approximation is initialized with an isotropic background conductivity equal to 1 S m^{-1}. The resulting background conductivity at the current position is then used to initialize the iterative process at the next position.

3.1 Borehole instrument sensitivity

The tri-axial induction tool consists of nine source–receiver configurations. In models with axial symmetry, only the co-axial components, H_{xx} and H_{yy}, and the co-planar component, H_{zz}, yield non-zero responses. Fig. 2 illustrates the sensitivity of these components for a homogeneous isotropic background conductivity of 1/30 S m^{-1}.

As the tool moves along the well trajectory, the averaging process yields a different background conductivity at each logging position. Consequently, the spatial sensitivity function varies with position, which in turn influences the accuracy of the discretization of the conductivity model. For computational efficiency, the subsurface should be discretized within a window that encompasses only the region with significant sensitivity, that is, when the changes of the sum of sensitivity function are only within 1 per cent as the ranges of grid blocks are expanded. Moreover, the grid resolution should be sufficiently refined to accurately capture the variability of the sensitivity function, particularly in the vicinity of the source and receiver locations where the sensitivity changes more rapidly.

To illustrate the effect of different simulation window settings, we consider adaptive Born simulations on model 1 at a frequency of 24 kHz and a transmitter–receiver spacing of 13.106 m. The conductivities are set to $\sigma_1 = 1/30$ S m^{-1} and $\sigma_2 = 1/2$ S m^{-1}. We performed the numerical computation over a moving window centred at the midpoint between the source and receiver locations. Fig. 3 illustrates the effect of varying the simulation domain size in the horizontal direction—39.014, 78.029 and 156.058 m—while keeping the size in the vertical direction and grid size fixed at 156.058 and 1.219 m, respectively. Results show that the simulation with a horizontal window size of 78.029 m closely matches that of the 156.058 m, suggesting that the majority of the sensitive area has been captured within the horizontal window size 78.029 m. Although the 39.014 m window yields a seemingly better match in some areas, its differences from

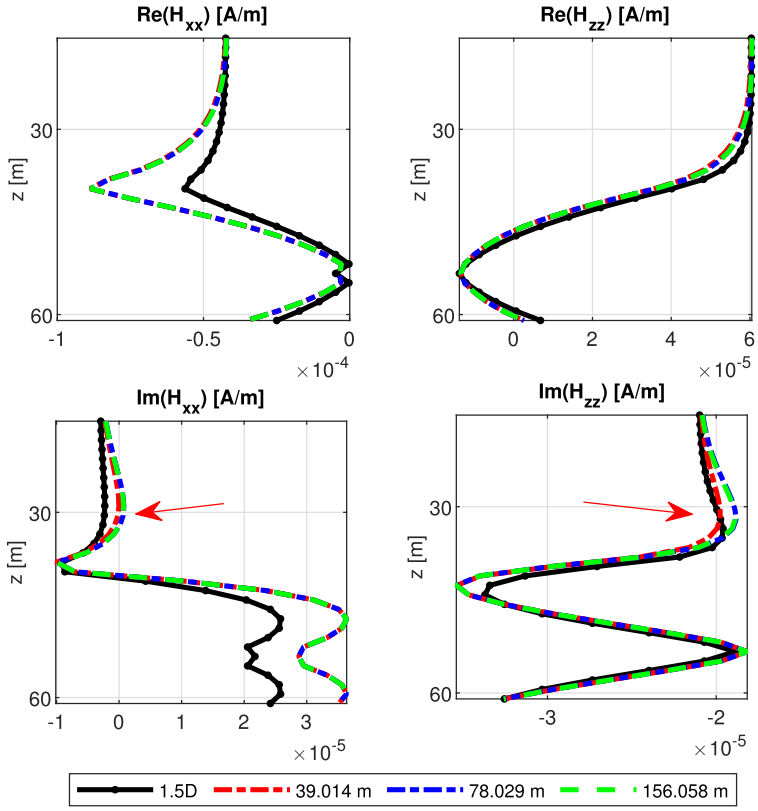

Figure 3. H_{xx} and H_{zz} components simulated with the adaptive Born approximation using different window sizes in the x- and y-directions: 39.014 m (red), 78.029 m (blue) and 156.058 m (green) from the tool midpoint. The size in the z-direction is fixed at 156.058 m for all cases. Real and imaginary parts are shown in the first and second row, respectively. Black lines represent the 1.5-D semi-analytical solution. Red arrows highlight qualitatively significant differences between the numerical solutions corresponding to different window sizes. The close agreement between blue and green lines indicates that the majority of the sensitive region has already been captured within the window horizontal size of 78.029 m.

the larger window results indicate that it has not captured the full extent of the significant sensitivity region. Fig. 4 shows the simulation results obtained using the same simulation window size of 78.029 m, but with varying grid sizes of 2.439, 1.219 and 0.3048 m. Results indicate that simulations with grid sizes of 1.219 and 0.3048 m yield similar trends, suggesting that a grid size of 1.219 m is adequately fine for this case. In these simulations, the H_{yy} component has the same value as the H_{xx} component and the cross components are below numerical precision; hence, they are not shown.

Ideally, the grid should also be adapted as the sensitivity function changes with the tool position. However, in this study, we show numerical results calculated using a fixed local window that moves along with the tool position for simplicity. This window consists of $64 \times 64 \times 128$ grid blocks with a grid size of 1.219 m, centred at the midpoint between the source and receiver location. We determine the window discretization value based on trial and error. This setting strikes a balance between accuracy and computation efficiency for our purpose, where the analysis of the results with a greater range and finer grid does not lead to a different conclusion.

3.2 Conductivity averaging method

In effective medium theory, different averaging schemes are employed depending on the relative orientation between the induced current density and the layering (S. Moskow *et al.* 1999; S. Davydycheva *et al.* 2003). In this context, the source and receiver orientation of the two field components, H_{xx} and H_{zz}, are associated with different electric field orientations relative to the layering. This motivates the investigation of different averaging methods in this subsection.

Eq. (14) expresses the arithmetic average of conductivity. Assuming the same weighting kernel can be used, we change the averaged quantity to perform a different type of averaging. For example, if we change both $\sigma^{(0,p)}$ and $\sigma^{(p)}$ to be their inverse $\left[\sigma^{(0,p)}\right]^{-1}$ and $\left[\sigma^{(p)}\right]^{-1}$, we will obtain a harmonic average. If we change these variables to their logarithmic forms, then we will have a geometric average.

In this example, we tested different averaging methods for computing the background conductivity. We use model 1 with the conductivity σ_1 and σ_2 set equal to 1/30 and 1/2 S m^{-1}, respectively. Fig. 5 shows the H_{xx} and H_{zz} components computed for this model using an adaptive Born approximation with arithmetic, harmonic, and geometric averages. Qualitatively, it can be observed that the results computed with the arithmetic average yield overall the best fit with the 1.5-D semi-analytical solution.

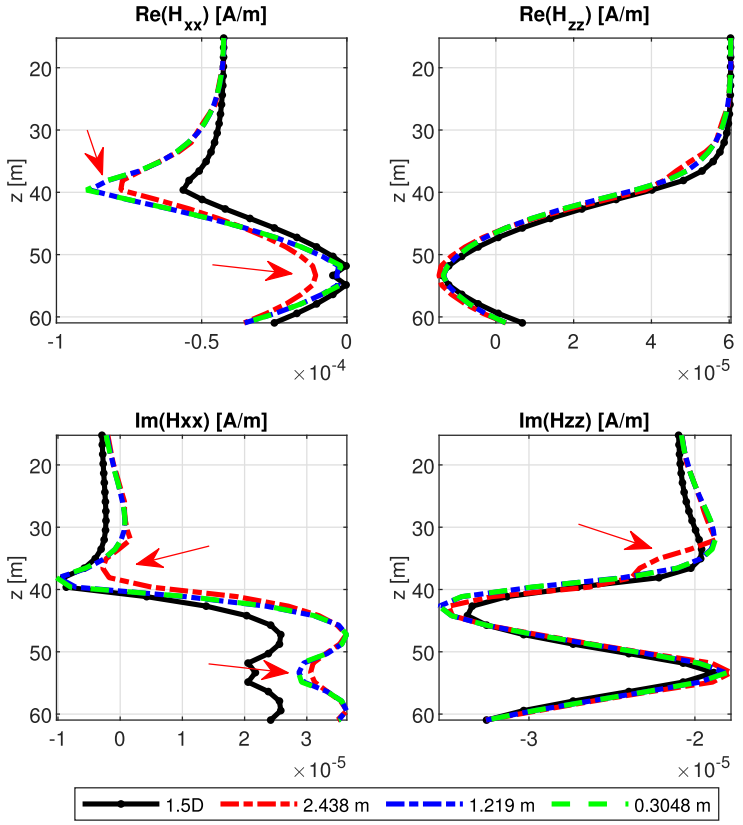

Figure 4. H_{xx} and H_{zz} components simulated with the adaptive Born approximation using different grid sizes of 2.438 (red), 1.219 (blue) and 0.3048 (green) m. Black lines represent the 1.5-D semi-analytical solution. Red arrows highlight qualitatively significant differences between the numerical solutions corresponding to different grid sizes. The similarity between the blue and green lines implies that grid refinement below 1.219 m may not lead to substantial improvements in accuracy.

Given that the arithmetic average yields overall the best fit with the 1.5-D solution, we will only show the average using the arithmetic conductivity in the remainder of this numerical experiment section.

3.3 Comparison to Born approximation using a fixed background

To evaluate the improvement offered by the adaptive Born approximation, we compare its simulation results to those obtained using a fixed background conductivity. Simulations were performed on model 1 and 2, which exhibit different conductivity transitions as the tool moves across the layers. In both models, the conductivity values of the two layers, σ_1 and σ_2, are set to 1/30 and 1/2 S m^{-1}. As comparisons to the adaptive Born approximation, we simulate the Born approximation with constant background conductivities equal to 1/30, 1/2 and 4/15 S m^{-1}, which correspond to the layers' conductivity and their arithmetic average. All numerical settings are kept identical for both the computation of adaptive and fixed Born approximations.

Figs 6 and 7 show the H_{xx} and H_{zz} components, respectively, for both models. Using the layer conductivity values as fixed backgrounds yields good agreement only in the homogeneous regions and up to a limited distance into the adjacent layer. Setting the average of layer conductivity as the background conductivity does improve the fixed Born approximation in the transition zone when the tool is entering/exiting the middle layer. However, it does not match well in the homogeneous area and the centre of the second layer. On the other hand, adaptively changing the background conductivity improves the overall matching between the Born approximation and the 1.5-D results. Notably, the H_{zz} component calculated using the adaptive Born approximation exhibits better agreement compared to the H_{xx} component in both models.

The background conductivities computed based on the sensitivities of different field components for both models are shown in Fig. 8. To identify the optimum real-valued isotropic background conductivity, we perform multiple Born approximations using background conductivity values ranging from 0.01 to 0.70 S m^{-1}. Overall, the optimum and adaptively selected background conductivities exhibit similar trends.

At the initial logging position, the background conductivities match the conductivity of the first layer for both the H_{xx} and H_{zz} components. As the tool approaches the second layer, the background conductivities begin to transition toward the second layer's conductivity and exhibit slight divergence between the two components. Upon exiting the second layer, the background conductivities

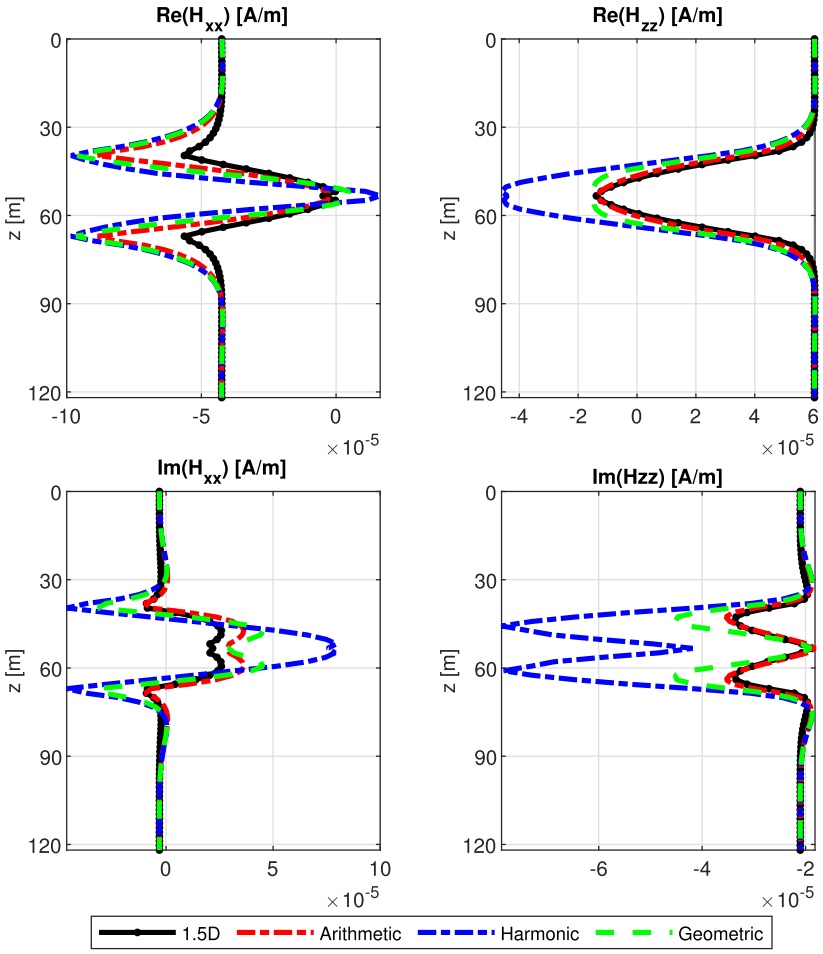

Figure 5. H_{xx} and H_{zz} components computed with different averaging methods: arithmetic (red), harmonic (blue) and geometric (green). Black lines identify the 1.5-D semi-analytical solution.

gradually evolve toward the third layer's conductivity, continuing until the second layer is outside the tool's sensitive region. Additionally, it is observed that the background conductivity begins to change earlier, approximately at $z = 15.24$ m for model 1, while for model 2, the transition starts at approximately $z = 30.48$ m. This indicates that the sensitivity range of the tool decreases with increasing conductivity.

3.4 Effects of various frequencies and spacings

Different frequencies and tool spacings provide different spatial patterns of the sensitivity function, particularly affecting the depth of investigation and resolution of the tool. To further assess the accuracy of the adaptive Born approximation, we investigated its performance under varying tool spacings and source frequencies.

We focus on model 1 with σ_1 and σ_2 are set to 1/30 and 1/2 S m^{-1}, respectively. Fig. 9 shows the relative difference between the adaptive Born approximation with the 1.5-D reference solution for a fixed tool spacing of 13.106 m using excitation frequencies of 2, 24 and 96 kHz. Whereas Fig. 10 is the same plot for a fixed frequency of 24 kHz for multiple receiver spacing of 7.010, 13.106 and 25.298 m. Overall, we observe that the error increases as the frequency increases for a fixed tool spacing. Similarly, the relative error also increases with an increase in tool spacing for a fixed frequency.

3.5 Effects of varying conductivity contrast

We consider model 1 and vary the contrast of the upper and lower resistive layers. Specifically, we set the conductivity of these layers equal to 1/3, 1/30 and 1/300 S m^{-1}, corresponding to contrast ratios of 1:1.5, 1:15 and 1:150 relative to the conductive layer in the middle. For comparison, we also show the result of the Born approximation with a constant background conductivity equal to the average of the resistive and conductive layer conductivity values.

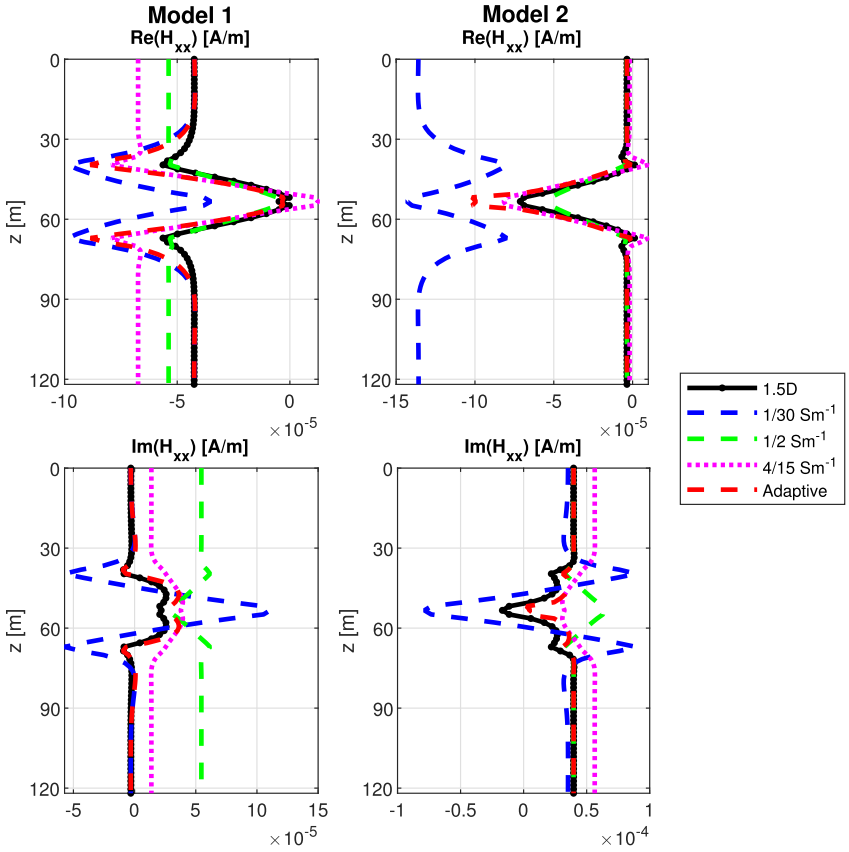

Figure 6. Simulation of H_{xx} for model 1 (left) and 2 (right). The Born approximation with a fixed background conductivity of 1/30 (blue), 1/2 (green) and 4/15 (magenta) S m^{-1}. Red and black lines identify the adaptive Born approximation and 1.5-D solution, respectively.

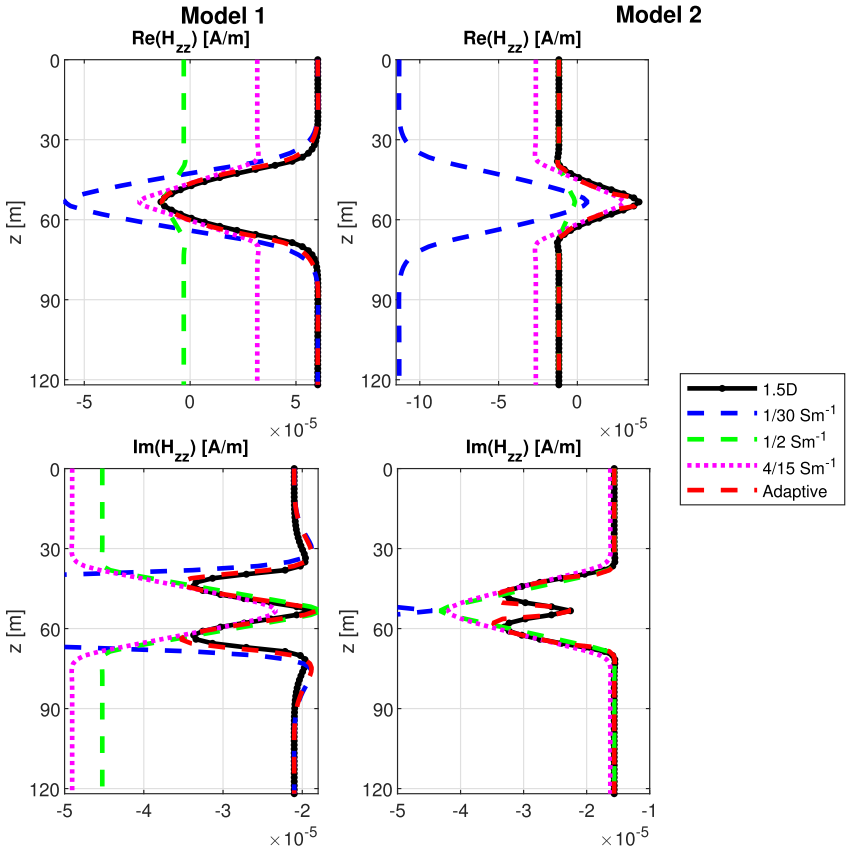

Figure 7. Simulation of H_{zz} for model 1 (left) and 2 (right). The Born approximation with a fixed background conductivity of 1/30 (blue), 1/2 (green) and 4/15 (magenta) S m^{-1}. Red and black lines identify the adaptive Born approximation and 1.5-D solution, respectively.

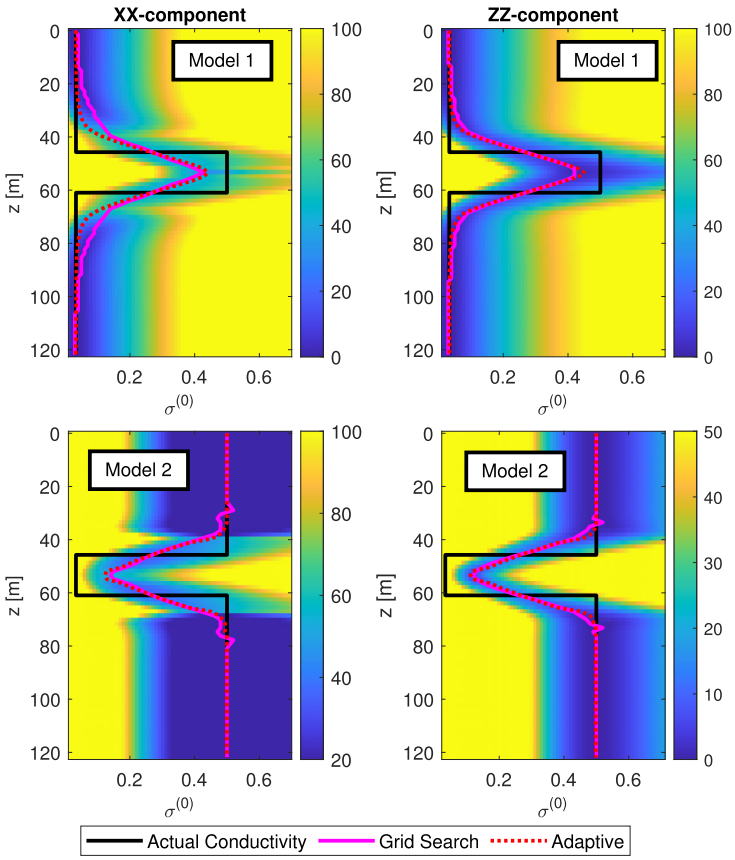

Figure 8. Background conductivity obtained from the averaging process at each logging position. The first and second columns indicate the average using the sensitivity of H_{xx} and H_{zz} components, respectively. The first and second rows correspond to models 1 and 2. The black lines indicate the true layer conductivities, and the red lines show the background conductivity obtained from the adaptive scheme. The colour scale represents the normalized absolute difference (in percentage) between the Born approximation and the 1.5-D solution for each depth and background conductivity, and the magenta lines mark the background conductivities that yield the minimum difference at each depth.

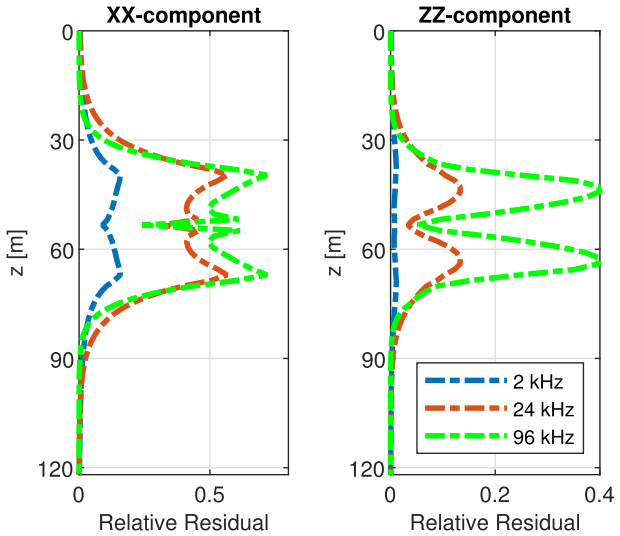

Figure 9. Difference between 1.5-D and adaptive Born approximation for a tool with 13.106 m spacing and varying frequency: 2 (blue), 24 (red) and 96 (green) kHz. The first and second columns are the relative residual for H_{xx} and H_{zz} configurations, respectively.

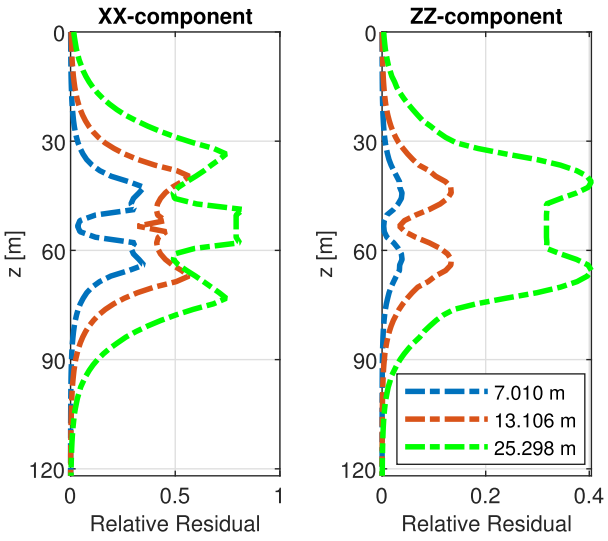

Figure 10. Difference between 1.5-D and adaptive Born approximation for tool with 24 kHz source frequency and varying spacing: 7.010 (blue), 13.106 (red) and 25.298 (green) m. The first and second columns are the relative residual for H_{xx} and H_{zz} configurations, respectively.

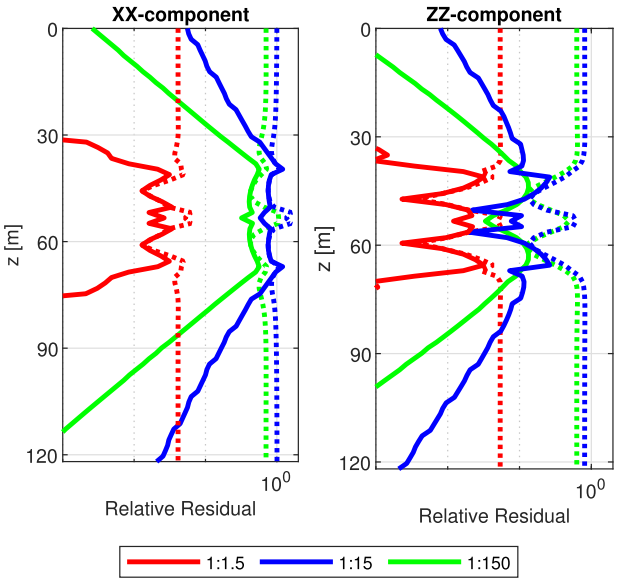

Figure 11. Relative difference between 1.5-D and adaptive Born approximation for varying contrast: 1/5 (solid red), 1/15 (solid green), and 1/150 (solid blue) relative to the middle layer. Dotted lines show the difference between the 1.5-D solution and the Born approximation with a fixed background conductivity, using the same colors to denote the corresponding contrasts. The first and second columns are the relative residual for H_{xx} and H_{zz} configurations, respectively.

The relative residual of the adaptive Born simulations for these cases with 24 kHz source frequency and 13.106 m tool spacing is shown in Fig. 11. We observe that the error, in general, increases with an increase in conductivity contrasts. From Fig. 12, we observe that the horn patterns in the H_{xx} component are still relatively close to the correct position, even though the magnitude is incorrect as the conductivity contrast increases. The pattern of the H_{zz} component shown in Fig. 13 still matches quite well in high contrast situations.

Fig. 14 shows the number of iterations before the average conductivity converges below the tolerance level. In all cases, the number of iterations increases as the distance of the tool from the layer interfaces decreases, similar to the trend of the changes in the error.

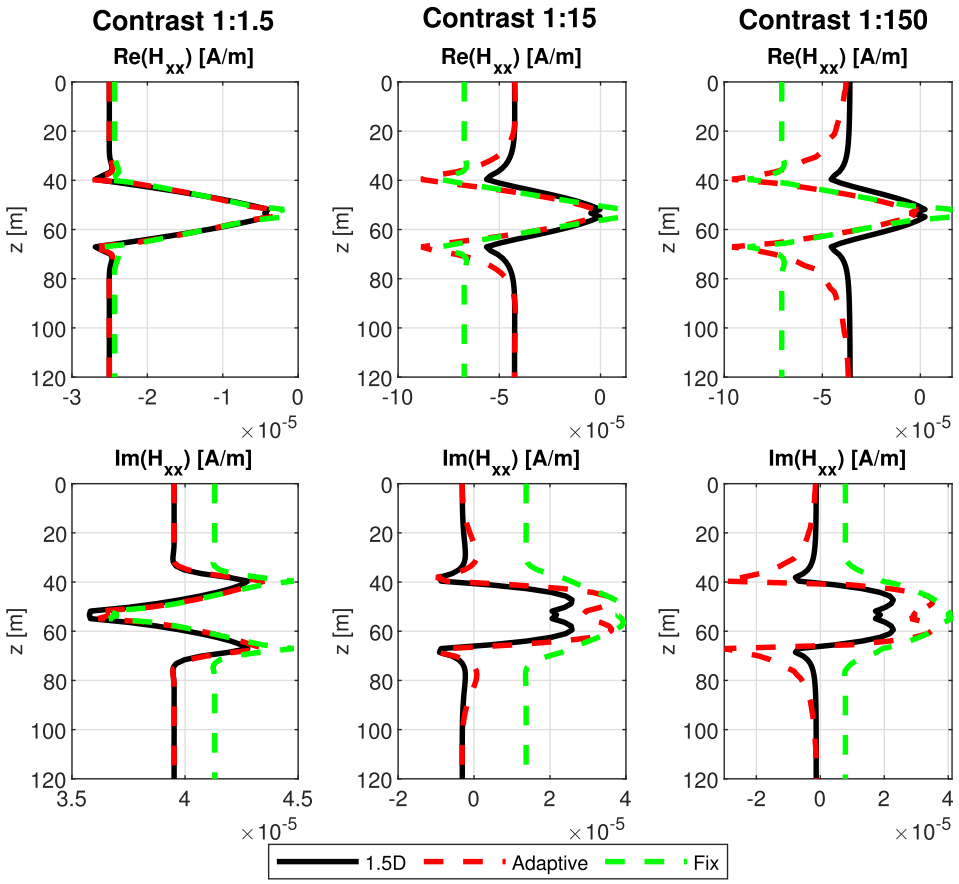

Figure 12. Simulation of H_{xx} for model 1 with varying contrast (from left to right): 1:5, 1:15 and 1:150 relative to the middle layer. Red, green and black lines identify the adaptive Born approximation, Born approximation with a fixed background conductivity and 1.5-D solution, respectively.

3.6 Effect of electrical anisotropy

Simulations were performed for a model where one of the layers exhibits VTI to investigate its effect on the performance of the adaptive Born approximation. We consider model 2 as shown in Fig. 1 and set the conductivity of the blue layers as the electrical anisotropic layers with horizontal and vertical conductivity equal to $\sigma_2^{(1)} = 1/2$ S m^{-1} and $\sigma_2^{(2)} = 1/5$ S m^{-1}, respectively.

Fig. 15 shows the magnetic field computed with the adaptive Born approximation using the Green's function defined for the isotropic and VTI media in the averaging process. The H_{zz} component is identical in both cases. The computed H_{xx} using the Green's function for an isotropic medium does not fit well in the homogeneous anisotropic area above and below the resistive layer.

The background conductivity obtained by both of these Green's functions is shown in Fig. 16. Because the H_{zz} component has zero sensitivity to the vertical conductivity in this case, only the horizontal conductivity is shown for the VTI Green's function. Subsequently, the background conductivity for the H_{zz} components computed using the VTI Green's function matches the one obtained using the isotropic Green's function. For the H_{xx} component, the isotropic Green's function returns an average of the horizontal and vertical conductivity, and it is closer to the horizontal conductivity in the homogeneous anisotropic regions in this example. On the other hand, the background conductivity computed with the VTI Green's function results in two different values for its horizontal and vertical components.

3.7 Complex versus absolute value of sensitivity as weight

In the previous results, we used the absolute value of sensitivity as the weight function in the averaging process. In principle, the averaging process can also be done by letting the sensitivity function described in eq. (16) as a complex-valued function. Fig. 17 shows the comparison of the H_{xx} and H_{zz} components calculated with complex and absolute value of the sensitivity function as the weight. For the results obtained using the complex (red) and absolute (blue) sensitivity-based isotropic Green's function, significant differences are observed in the imaginary part of both components, marked by the red arrows. Qualitatively, the imaginary parts of H_{xx} with the absolute value of sensitivity are more similar compared to the one with a complex value of sensitivity. Another interesting feature of using the absolute value of sensitivity is that the background conductivity computed with the VTI Green's function (magenta) yields

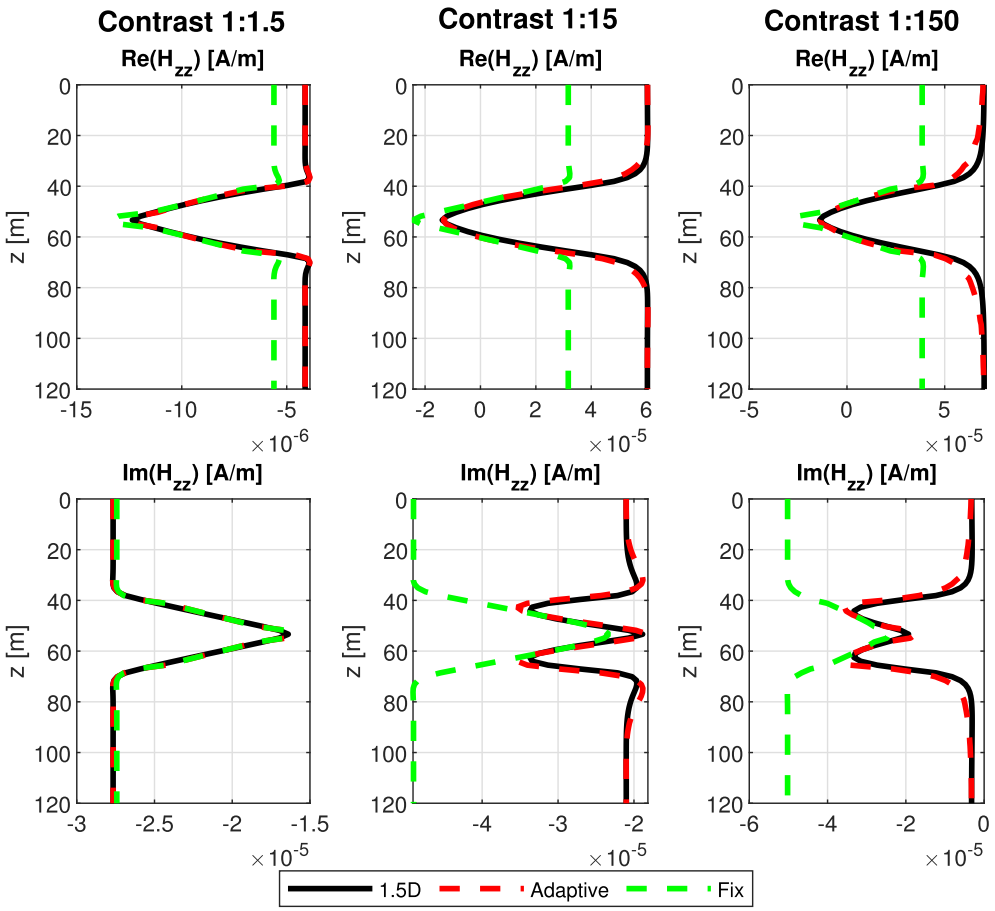

Figure 13. Simulation of H_{zz} for model 1 with varying contrast (from left to right): 1:5, 1:15 and 1:150 relative to the middle layer. Red, green and black lines identify the adaptive Born approximation, Born approximation with a fixed background conductivity and 1.5-D solution, respectively.

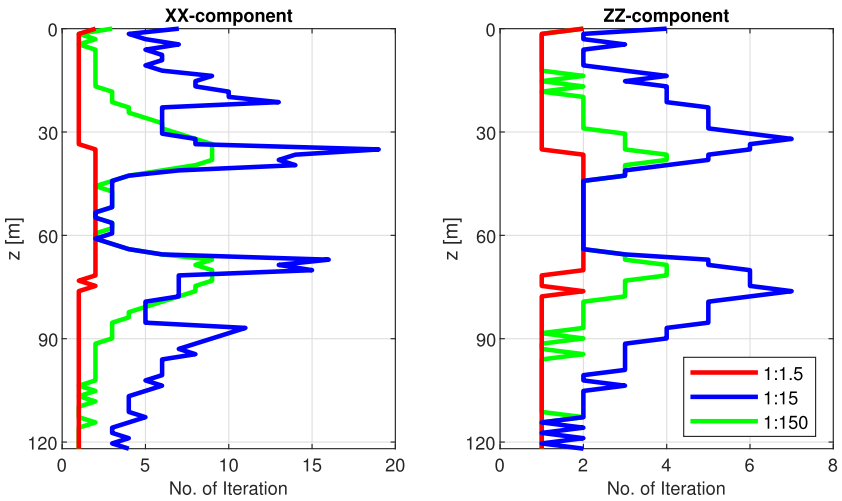

Figure 14. Number of iterations of adaptive Born approximation for varying contrast: 1:5 (red), 1:15 (green) and 1:150 (blue) relative to the middle layer. The first and second columns are the relative residual for H_{xx} and H_{zz} components, respectively.

similar results to the isotropic Green's function (blue) when applied to an isotropic model. On the other hand, the one with complex-valued sensitivity based on the VTI Green's function (green) provides a different result, which is not necessarily better.

However, the difference in background conductivity for each component is more apparent when the weight of the average is the complex-valued sensitivity, as shown in Fig. 18, compared to the one with the absolute value shown in Fig. 8.

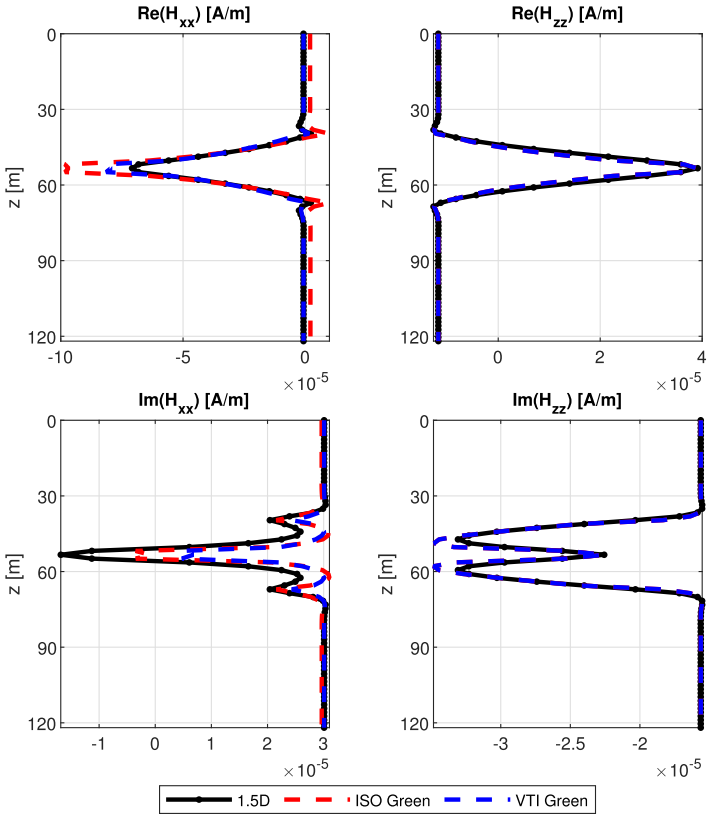

Figure 15. H_{xx} and H_{zz} components calculated from model 2 with anisotropic upper and lower layer. Red and blue lines identify the adaptive Born approximation using isotropic and VTI Green's functions, respectively. Black lines identify the 1.5-D solution.

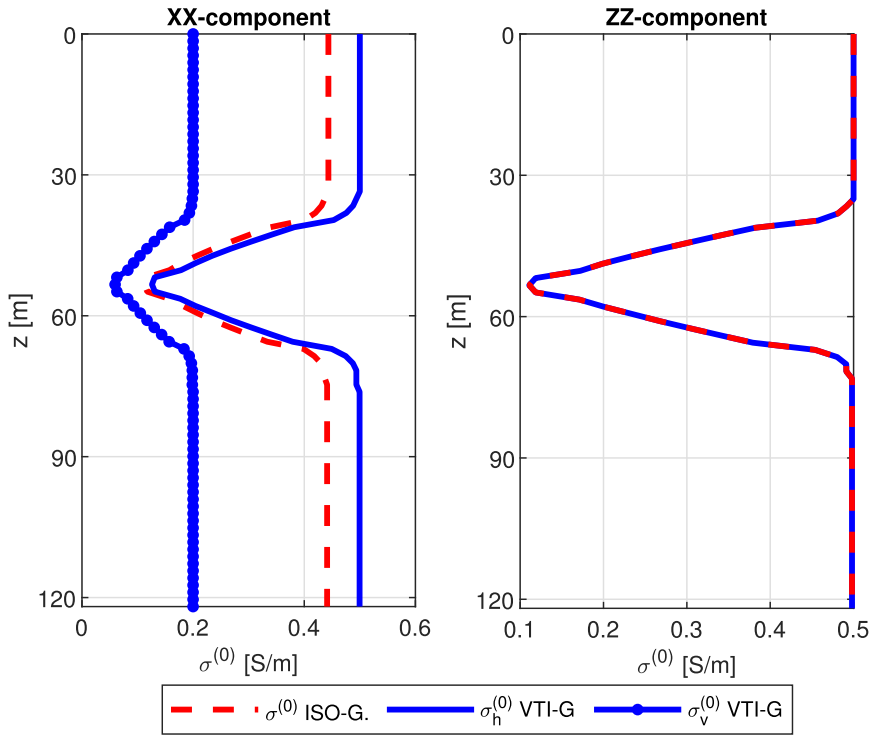

Figure 16. Background conductivity for the H_{xx} (left) and H_{zz} (right) components for the case of an anisotropic model. Dashed red lines identify the background conductivity obtained using an isotropic model. Horizontal and vertical background conductivity obtained using the VTI Green's function are identified with the solid and dotted blue lines, respectively.

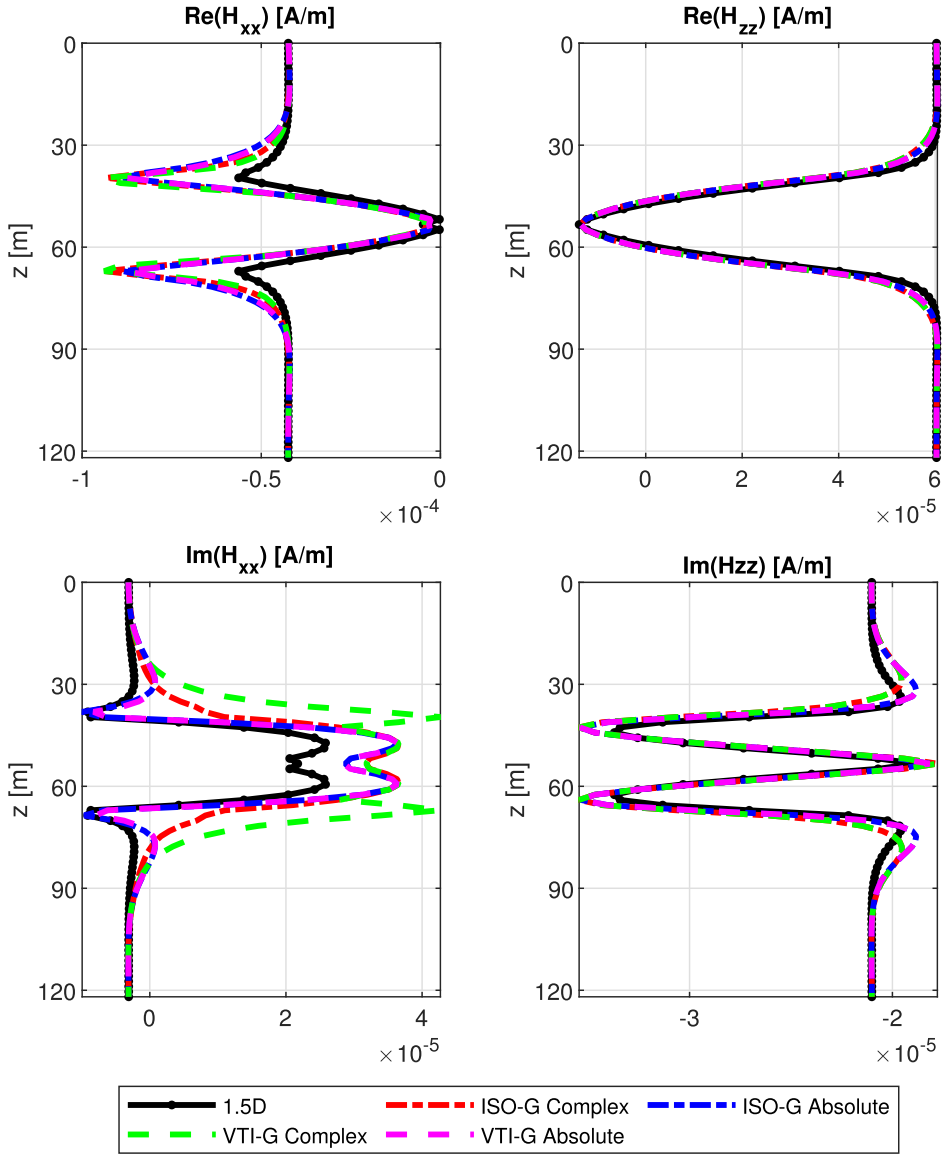

Figure 17. Comparison of H_{xx} and H_{zz} components with the background conductivity averaged using complex (red) and absolute (blue) value of the sensitivity function based on the isotropic Green's function. Green and magenta lines identify the results obtained using complex and absolute value of the sensitivity function based on the VTI Green's function, respectively.

3.8 Example of a 3-D model

Fig. 19 shows the conductivity model of a faulted layered medium, following the description in W. Saputra *et al.* (2025). The fault has a dip and azimuth of 45°, resulting in 3-D structures where the fault plane intersects the layer interfaces. Both the footwall and hanging wall consist of five layers with the same conductivity values. From top to bottom, the horizontal conductivities are 1/2, 1/30, 1/1.5, 1/30 and 1/1.5 S m^{-1}, while the vertical conductivities are 1/5, 1/30, 1/4, 1/30 and 1/4 S m^{-1}. The thicknesses of the three middle layers are 18.288, 3.048 and 9.144 m, respectively. The top of the footwall is located at $z = 0$ m and the fault shifts the hanging wall downward by 15.24 m. A vertical well is placed at $x = 621.5$ m and it intersects with the fault plane at $z = 15.1101$ m.

We simulated the response of an induction tool with a frequency of 24 kHz and a source–receiver spacing of 13.106 m along the vertical well. As a reference, we use the results obtained from the full IE method, where the internal electric field is computed by solving the discretized form of eq. (3) using an iterative solver with the same numerical settings as those used for the adaptive and fixed Born approximation. For this reference solution, the background conductivity is set to 7/20 S m^{-1}, which corresponds to the average of the minimum and maximum conductivities in the model. The adaptive and fixed Born approximations are computed using the Green's function for a homogeneous VTI background medium. For the fixed Born approximation, the background conductivity is taken as the average of the minimum and maximum values of the horizontal and vertical components, which are equal to 7/20 and 17/120 S m^{-1}, respectively.

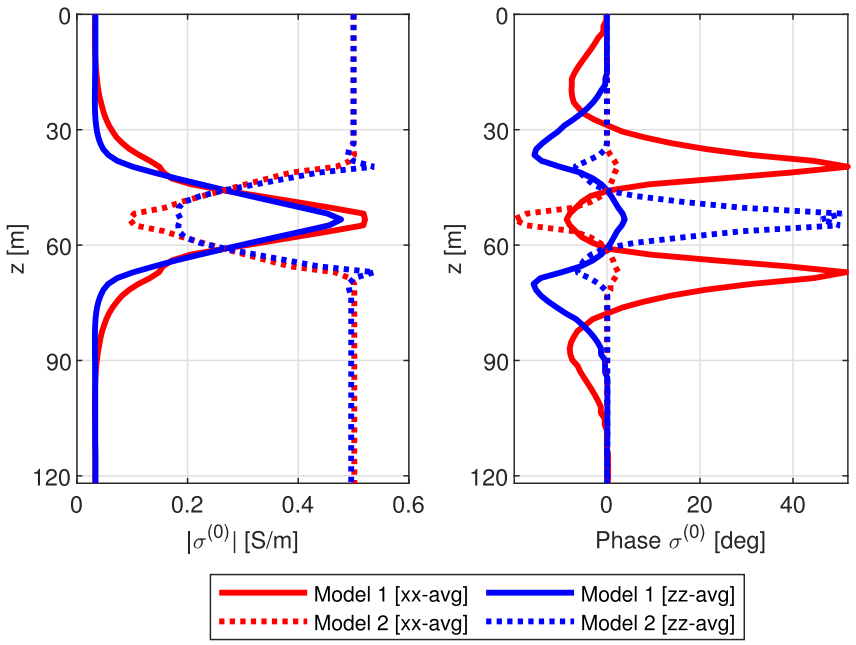

Figure 18. Absolute value (left) and phase (right) of the conductivity average (background conductivity) at each logging position. Red and blue lines identify the average using the sensitivity H_{xx} and H_{zz} components based on the isotropic Green's function. The average of models 1 and 2 are shown with solid and dotted lines, respectively.

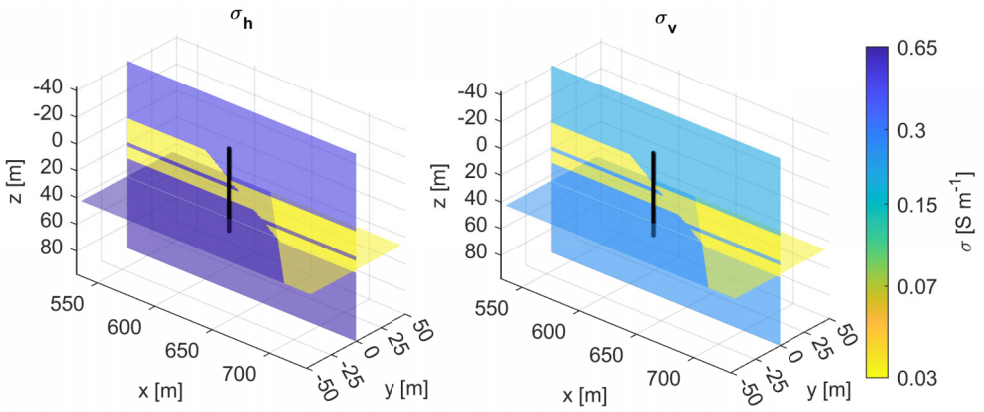

Figure 19. Example of a horizontally layered media deformed with a 3-D fault. Black dots indicate the logging positions.

The co-components (H_{xx} and H_{zz} components) and the cross-components (H_{yx}, H_{zx} and H_{yz} components) of the simulation results are shown in Figs 20 and 21, respectively. Only three cross-components are shown due to the others having the same value as the one shown in Fig. 21: $H_{xy} = H_{yx}$, $H_{zy} = H_{zx}$ and $H_{yz} = H_{xz}$ components. Overall, the adaptive Born approximation indicates a better agreement with the full IE solution compared to the one with a fixed background conductivity, especially in the co-components.

4 DISCUSSION

We have developed an adaptive Born approximation for modelling borehole EM induction measurements. In this study, we focus on a simple test case involving a vertical well intersecting a three-layer formation to verify and benchmark the method. Compared to using a fixed background conductivity, such as a simple average of unique conductivity values, our adaptive approach improved the accuracy of the Born approximation. In regions where the tool is insensitive to heterogeneity, the adaptive Born approximation naturally returns the analytical response of a homogeneous medium. In heterogeneous regions, the adaptive Born approximation can be more than twice as accurate as the fixed-background approach. At certain locations, the accuracy of both approaches is similar because the adaptive averaging process yields a background conductivity close to the fixed value. The improvement of the adaptive Born approximation can also be observed in the special case with a simple 3-D structure. This observation verifies the applicability of the adaptive Born approximation for 3-D modelling of borehole EM induction measurements.

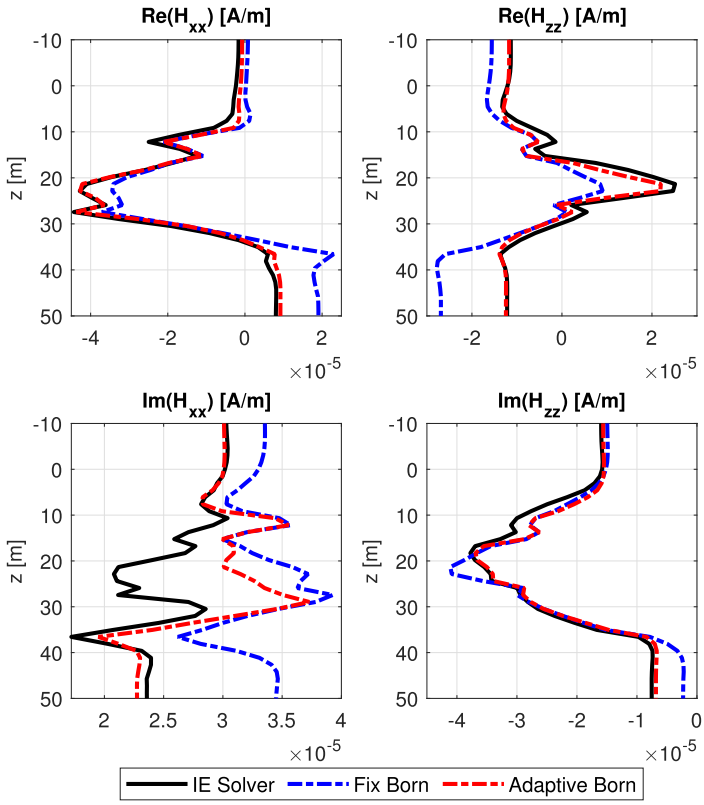

Figure 20. H_{xx} and H_{zz} components calculated from the 3-D faulted horizontally layered media. Red and blue lines identify the fields calculated using adaptive and fixed Born approximations, respectively. Black lines identify the magnetic fields calculated with electric fields obtained by solving the IE using an iterative solver and a fixed background conductivity.

Due to the alignment of the source and receiver being either parallel or perpendicular to layering, we expect the choice of the averaging scheme to depend on the source and receiver orientation. However, based on the observed best-fitting averaging method for the H_{xx} and H_{zz} components, the conductivity averaging does not directly follow the intuition derived from effective medium theory. One possible explanation for the superior performance of the arithmetic average is that its form, as shown in eq. (14), more closely resembles the structure of the scattered field in eq. (12), which implicitly reflects the spatial weighting of conductivity.

Although the use of a complex-valued sensitivity function is, in principle, more consistent with the mathematical form of the scattered field, our numerical results in subsection 3.7 do not indicate improved performance compared to using an absolute-valued sensitivity. Allowing the averaging weights to be complex-valued can result in a complex-valued background conductivity that may fall outside the actual conductivity range in the transition zone. Introducing an imaginary component into a medium that is physically real-valued effectively adds an artificial contrast, which contradicts the weak-scattering assumption underlying the Born approximation. In contrast, using the absolute-valued sensitivity as the weighting function ensures a real-valued background conductivity that remains within the bounds of the actual conductivity distribution, thus maintaining consistency with the physical assumptions of the model.

For the implementation in anisotropic media, the use of an isotropic Green's function in the averaging process fails to yield magnetic fields consistent with the homogeneous anisotropic background. Nevertheless, averaging results across different measurement configurations interestingly capture components associated with different directions of the anisotropic conductivity tensor. Conversely, the results presented in subsection 3.7 indicate that when the Green's function is defined using a VTI background, it can yield a background conductivity similar to that obtained using the isotropic Green's function. Ideally, the Green's function defined for fully anisotropic and/or heterogeneous media should be employed in the calculations. However, such a Green's function either lacks a closed-form expression in the spatial domain or presents substantial challenges in terms of numerical implementation and computational cost. Therefore, even though we implemented the Green's function for VTI media, the Green's function for isotropic homogeneous media remains attractive due to its simpler singularity structure, facilitating integration with iterative solvers.

We verified the limitations of the adaptive Born approximation through numerical experiments. Our results show that the accuracy of the approximation decreases with increasing spacing, frequency and conductivity contrast. Furthermore, convergence requires more iterations when dealing with high-contrast transitions. In the contrast variation tests, we observed that the adaptive Born approximation tends to exaggerate the 'horn' effect in the transition zone as the electrical conductivity contrast increases. Nevertheless, the magnetic field pattern as the tool moves is still somewhat preserved. This is a promising observation to investigate further in inversion/imaging:

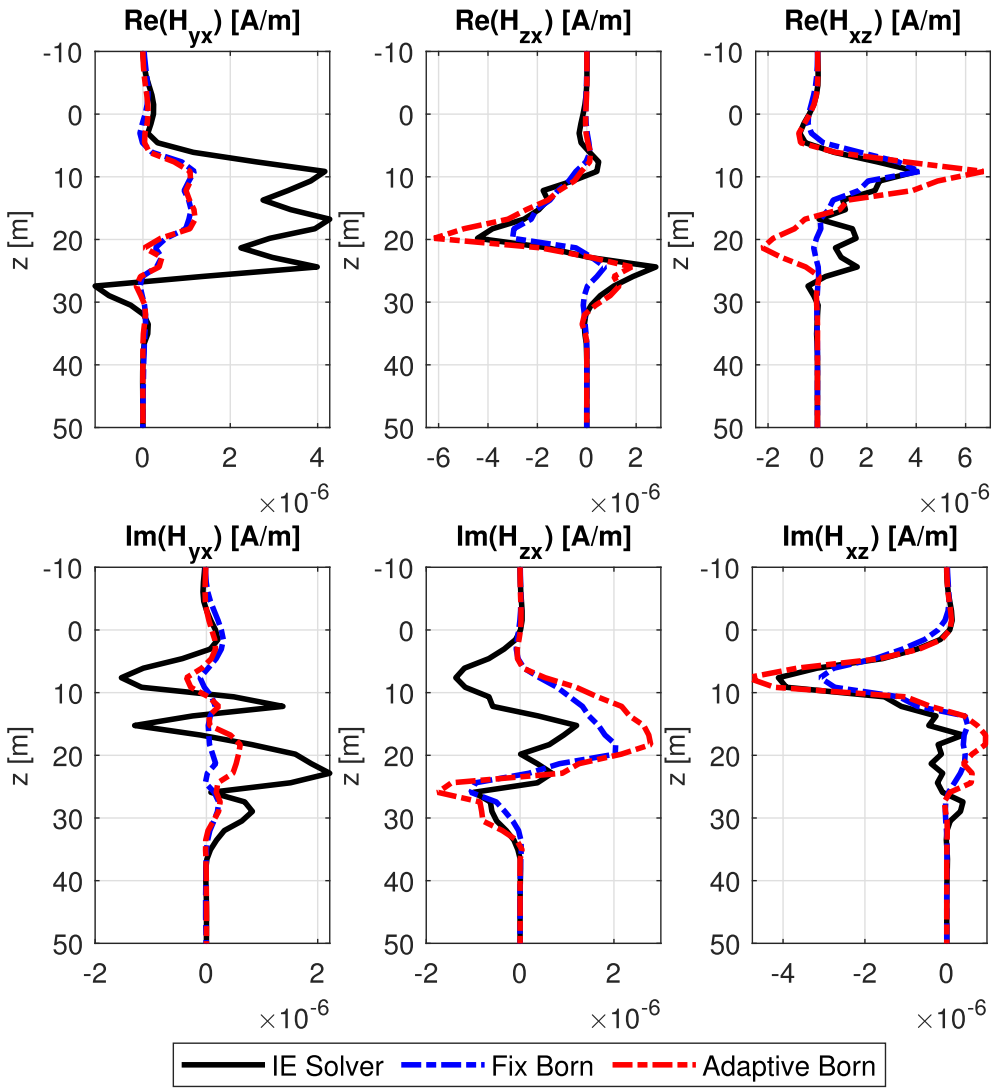

Figure 21. H_{yx}, $H_{zx}$and H_{xz} components calculated from the 3-D faulted horizontally layered media. Red and blue lines identify the fields calculated using adaptive and fixed Born approximations, respectively. Black lines identify the magnetic fields calculated with electric fields obtained by solving the IE using an iterative solver and a fixed background conductivity.

whether the preserved field pattern leads to a reliable reconstruction of the structure—despite inaccurate contrast—or whether it results in a completely distorted inverted model.

5 CONCLUSIONS

We introduced a new implementation of the adaptive Born approximation for modelling borehole EM measurements. In this method, the background conductivity is adaptively chosen as a weighted average of the conductivity distribution surrounding the tool. Using the sensitivity function as the weight of the average, the averaging process naturally takes into account the reduced contribution of the medium farther away from the tool position. In addition, it also considers different sensitivity patterns for each measurement configuration and frequency.

We conducted a series of experiments to investigate the behaviour of the adaptive Born approximation in simplified settings. Overall, this approximation yields significantly better agreement with the reference solution compared to the conventional Born approximation, which assumes a fixed background conductivity throughout the entire logging interval. In some cases, the error associated with the conventional Born approximation exceeds that of the adaptive approach by more than an order of magnitude, depending on the local characteristics of the model. The main limiting factors for the accuracy of the adaptive Born approximation are frequency, transmitter–receiver spacing and conductivity contrast.

While the adaptive background update involves iterative optimization, each iteration only requires numerical integration. In this study, we adopt a simple Riemann numerical integration, which entails simple additions and multiplications with computational time

complexity and memory usage of $\mathcal{O}(n)$ with n the number of grid points. By comparison, an iterative solver using the IE method with FFT has the computational complexity of $\mathcal{O}(n \log n)$ per iteration. As an example of computation time, in the high-contrast condition we described—which required more iterations than other cases—it took approximately one CPU/GPU minute to compute the magnetic fields at 81 positions sequentially. It should be noted that we use a fixed numerical setting, which is ideally also adapted based on the spatial sensitivity function for a given background conductivity.

This study focuses exclusively on the foundational study of the adaptive Born approximation in simplified settings. We only consider the situation of a vertical angle and axis-symmetric model. Under those conditions, the interaction of the cross-components is ignored, and there is no need for the projection of the magnetic field components into the principal axes of layering. Even though the method is, in principle, applicable for a general 3-D structure, the effect of borehole angle on the performance and best implementation of adaptive Born approximation remains an important topic for further improving the approximation.

Striking a well-balanced trade-off between computational speed and solution accuracy is essential in real-time imaging conditions with tight operational constraints. In this context, integrating the adaptive Born approximation as a fast, approximate solution for subsurface imaging from borehole EM measurements in 3-D settings provides a promising direction for future research. It can serve as an effective prior for more computationally expensive 3-D inversions that require higher forward modelling accuracy. By enabling rapid updates of the subsurface model while drilling, this approach can robustly support well geosteering operations—helping to make timely decisions for well trajectory adjustments and optimal reservoir navigation.

ACKNOWLEDGMENTS

This work is part of the Center for Research-based Innovation DigiWells: Digital Well Center for Value Creation, Competitiveness and Minimum Environmental Footprint (NFR SFI project no. 309589, https://DigiWells.no). The center is a cooperation of NORCE Norwegian Research Centre AS, the University of Stavanger, the Norwegian University of Science and Technology (NTNU) and the University of Bergen. It is funded by Aker BP, ConocoPhillips, Equinor, Energy, TotalEnergies, Vår Energi, Harbour Energy and the Research Council of Norway. The 1-D data shown in this work originate from the code developed by the Formation Evaluation Research Consortium at the University of Texas at Austin. The authors would like to acknowledge the involvement in the 3-D-GIG project: 3-D geological interpretation for geosteering of wells project (Project no. 336385).

DATA AVAILABILITY

Currently, the data and codes relating to this work are not freely available. We are considering publishing the codes with an open-source license in the future.

REFERENCES

Abubakar, A. & Habashy, T.M., 2006. A closed-form expression of the electromagnetic tensor green's functions for a homogeneous ti-anisotropic medium, *IEEE Geosci. Remote Sens. Lett.,* **3**(4), 447–451.

Antonsen, F., Danielsen, B.E., Jensen, K.R., Prymak-Moyle, M., Lotsberg, J.K., Teixeira De Oliveira, M.E. & Constable, M.V., 2022. What next after a decade with significant advances in the application of ultradeep azimuthal resistivity measurements?, *Petrophysics,* **63**(06), 762–780.

Avdeev, D.B., Kuvshinov, A.V., Pankratov, O.V. & Newman, G.A., 2002. Three-dimensional induction logging problems, part i: An integral equation solution and model comparisons, *Geophysics,* **67**(2), 413–426.

Bensdorp, S., Petersen, S.A., van den Berg, P.M. & Fokkema, J.T., 2014. An approximate 3D computational method for real-time computation of induction logging responses, *Geophysics,* **79**(3), E137–E148.

Christensen, N.B., 1997. Electromagnetic subsurface imaging. A case for an adaptive Born approximation, *Surv. Geophys.,* **18,** 477–510.

Clegg, N. *et al.* , 2022. Ultra-deep 3D electromagnetic inversion for anisotropy, a guide to understanding complex fluid boundaries in a turbidite reservoir, in *SPWLA Annual Logging Symposium,* SPWLA, p. D031S002R005. doi: 10.30632/SPWLA-2022-0119.

Davydycheva, S., Druskin, V. & Habashy, T.M., 2003. An efficient finite-difference scheme for electromagnetic logging in 3D anisotropic inhomogeneous media, *Geophysics,* **68**(5), 1525–1536.

Elkhamry, A., Clegg, N., Taher, A. & Bikchandaev, E., 2023. The first successful azimuthal well placement utilizing real-time azimuthal resistivity measurements and Ultra-Deep 3D inversion, in *International Petroleum Technology Conference,* IPTC, p. D012S006R001. doi: 10.2523/IPTC-22779-EA.

Fang, S., Gao, G. & Verdin, C.T., 2006. Efficient 3D electromagnetic modelling in the presence of anisotropic conductive media, using integral equations, *Explor. Geophys.,* **37**(3), 239–244.

Gao, G., Torres-Verdin, C. & Habashy, T.M., 2005. Analytical techniques to evaluate the integrals of 3D and 2D spatial dyadic Green's functions, *Progr. Electromagn. Res.,* **52,** 47–80.

Gibson, W.C., 2021. *The Method of Moments in Electromagnetics,* CRC Press.

Habashy, T. & Abubakar, A., 2007. A generalized material averaging formulation for modelling of the electromagnetic fields, *J. Electromagn. Waves Appl.,* **21**(9), 1145–1159.

Habashy, T.M., Groom, R.W. & Spies, B.R., 1993. Beyond the Born and Rytov approximations: A nonlinear approach to electromagnetic scattering, *J. geophys. Res.: Solid Earth,* **98**(B2), 1759–1775.

Hohmann, G.W., 1983. Three-dimensional EM modeling, *Geophys. Surv.,* **6**(1), 27–53.

Hou, J., Mallan, R.K. & Torres-Verdín, C., 2006. Finite-difference simulation of borehole EM measurements in 3D anisotropic media using coupled scalar-vector potentials, *Geophysics,* **71**(5), G225–G233.
Hursan, G. & Zhdanov, M.S., 2002. Contraction integral equation method in three-dimensional electromagnetic modeling, *Radio Sci.,* **37**(6), 1–13.
Jakobsen, M. & Tveit, S., 2018. Distorted Born iterative T-matrix method for inversion of CSEM data in anisotropic media, *Geophys. J. Int.,* **214**(3), 1524–1537.
Jakobsen, M., Xiang, K. & van Dongen, K.W.A., 2023. Seismic and medical ultrasound imaging of velocity and density variations by nonlinear vectorial inverse scattering, *J. acoust. Soc. Am.,* **153**(5), 3151–3151.
Key, K. & Ovall, J., 2011. A parallel goal-oriented adaptive finite element method for 2.5-d electromagnetic modelling, *Geophys. J. Int.,* **186**(1), 137–154.
Moskow, S., Druskin, V., Habashy, T., Lee, P. & Davydycheva, S., 1999. A finite difference scheme for elliptic equations with rough coefficients using a cartesian grid nonconforming to interfaces, *SIAM J. Numer. Anal.,* **36**(2), 442–464.
Pardo, D., Matuszyk, P.J., Puzyrev, V., Torres-Verdin, C., Nam, M.J. & Calo, V.M., 2021. *Modeling of Resistivity and Acoustic Borehole Logging Measurements Using Finite Element Methods,* Elsevier.
Ren, Z., Kalscheuer, T., Greenhalgh, S. & Maurer, H., 2013. A goal-oriented adaptive finite-element approach for plane wave 3-d electromagnetic modelling, *Geophys. J. Int.,* **194**(2), 700–718.
Saputera, D.H., Jakobsen, M., van Dongen, K. W.A., Jahani, N., Eikrem, K.S. & Alyaev, S., 2024. 3-D induction log modelling with integral equation method and domain decomposition pre-conditioning, *Geophys. J. Int.,* **236**(2), 834–848.
Saputera, D.H., Jakobsen, M., van Dongen, K.W.A. & Jahani, N., 2025. Sequential multi-dimensional parameter inversion of induction logging data, *Geophys. Prospect.,* **73**(4), 1315–1332.
Saputra, W. *et al.* , 2025. Recent developments and verifications for the multi-dimensional and data-adaptive interpretation of borehole udar measurements , in *SPWLA Annual Logging Symposium,* SPWLA, p. D051S021R002. doi: 10.30632/SPWLA-2025-0102.
Shahriari, M., Rojas, S., Pardo, D., Rodríguez-Rozas, A., Bakr, S.A., Calo, V.M. & Muga, I., 2018. A numerical 1.5 D method for the rapid simulation of geophysical resistivity measurements, *Geosciences,* **8**(6), 225.
Singer, B.S., Mezzatesta, A. & Wang, T., 2003. Integral equation approach based on contraction operators and krylov subspace optimisation, *ASEG Extended Abstracts,* **2003**(1), 1–14.
Torres-Verdin, C. & Habashy, T.M., 1994. Rapid 2.5-dimensional forward modeling and inversion via a new nonlinear scattering approximation, *Radio Sci.,* **29**(04), 1051–1079.
Wilson, G., Marchant, D., Haber, E., Clegg, N., Zurcher, D., Rawsthorne, L. & Kunnas, J., 2019. Real-time 3D inversion of ultra-deep resistivity logging-while-drilling data, in *SPE Annual Technical Conference and Exhibition,* SPE. doi: 10.2118/196141-MS.
Zwamborn, P. & van den Berg, P.M., 1992. The three-dimensional weak form of the conjugate gradient FFT method for solving scattering problems, *IEEE Trans. Microwave Theory Techn.,* **40**(9), 1757.

DYADIC GREEN'S FUNCTION

The dyadic Green functions are the solutions of Maxwell's equations for a point source. For a VTI medium, the background conductivity tensor is written as

$$\boldsymbol{\sigma}^{(0)} = \begin{bmatrix} \sigma_h^{(0)} & 0 & 0 \\ 0 & \sigma_h^{(0)} & 0 \\ 0 & 0 & \sigma_v^{(0)} \end{bmatrix}, \tag{A1}$$

where $\sigma_{h,v}^{(0)}$ are the horizontal and vertical components of the background conductivity. The Green's function for the VTI medium as a function of space in this appendix follows the expression in A. Abubakar & T.M. Habashy (2006). First, we define the following quantities:

$$r = |\mathbf{x}| = \sqrt{x^2 + y^2 + z^2}, \tag{A2}$$
$$R = \sqrt{x^2 + y^2 + \lambda^2 z^2}, \tag{A3}$$
$$\lambda = \sqrt{\frac{\sigma_h}{\sigma_v}}, \tag{A4}$$
$$g_h = \frac{e^{ik_h r}}{4\pi r}, \tag{A5}$$
$$g_v = \lambda \frac{e^{ik_v R}}{4\pi R}, \tag{A6}$$
$$k_{h,v} = \sqrt{i\omega\mu_0\sigma_{h,v}^{(0)}}. \tag{A7}$$

Then, the dyadic Green's function for the electric $\mathbf{G}^{EE}(\mathbf{x}, \omega)$ and magnetic $\mathbf{G}^{HE}(\mathbf{x}, \omega)$ fields due to electric current source can be written in the form

$$\mathbf{G}^{EE}(\mathbf{x}, \omega) = i\omega\mu_0 \begin{bmatrix} g_h & 0 & 0 \\ 0 & g_h & 0 \\ \frac{xz}{x^2+y^2}(g_h - g_v) & \frac{yz}{x^2+y^2}(g_h - g_v) & g_v \end{bmatrix} - \nabla \begin{bmatrix} \Phi_x^E \\ \Phi_y^E \\ \Phi_z^E \end{bmatrix}, \tag{A8}$$
$$\mathbf{G}^{HE}(\mathbf{x}, \omega) = \tfrac{1}{i\omega\mu_0} \nabla \times \mathbf{G}^{EE}(\mathbf{x}, \omega), \tag{A9}$$

with

$$\Phi_x^E(\mathbf{x}, \omega) = \tfrac{x}{4\pi\sigma_h} \left\{ \tfrac{ik_h}{x^2+y^2} \left[e^{ik_v R} - e^{ik_h r} \right] + \tfrac{\lambda}{R^3}(1 - ik_v R) e^{ik_v R} \right\}, \tag{A10}$$
$$\Phi_y^E(\mathbf{x}, \omega) = \tfrac{y}{4\pi\sigma_h} \left\{ \tfrac{ik_h}{x^2+y^2} \left[e^{ik_v R} - e^{ik_h r} \right] + \tfrac{\lambda}{R^3}(1 - ik_v R) e^{ik_v R} \right\}, \tag{A11}$$

$$\Phi_z^E(\mathbf{x},\omega) = \tfrac{\lambda}{4\pi\sigma_v}\tfrac{z}{R^3}(1-ik_vR)e^{ik_vR}. \tag{A12}$$

Whereas the dyadic Green's functions for the magnetic and electric field due to magnetic current sources are given by

$$\mathbf{G}^{HH}(\mathbf{x},\omega) = -\begin{bmatrix}\sigma_v & 0 & 0\\ 0 & \sigma_v & 0\\ 0 & 0 & \sigma_h\end{bmatrix}\begin{bmatrix} g_v & 0 & 0\\ 0 & g_v & 0\\ \frac{xz}{x^2+y^2}(g_v-g_h) & \frac{yz}{x^2+y^2}(g_v-g_h) & g_h\end{bmatrix} + \nabla\begin{bmatrix}\Phi_x^H\\ \Phi_y^H\\ \Phi_z^H\end{bmatrix}, \tag{A13}$$

$$\mathbf{G}^{EH}(\mathbf{x},\omega) = \frac{1}{\sigma_h}\nabla\times\mathbf{G}^{HH}(\mathbf{x},\omega), \tag{A14}$$

with

$$\Phi_x^H(\mathbf{x},\omega) = \frac{x}{i4\pi\omega\mu}\left\{\frac{ik_h}{x^2+y^2}\left[e^{ik_hR}-e^{ik_vR}\right]+\frac{1}{r^3}(1-ik_hr)e^{ik_hr}\right\}, \tag{A15}$$

$$\Phi_y^H(\mathbf{x},\omega) = \frac{y}{i4\pi\omega\mu}\left\{\frac{ikh}{x^2+y^2}\left[e^{ik_hR}-e^{ik_vR}\right]+\frac{1}{r^3}(1-ik_hr)e^{ik_hr}\right\}, \tag{A16}$$

$$\Phi_z^H(\mathbf{x},\omega) = \frac{1}{i4\pi\omega\mu}\frac{z}{r^3}(1-ik_hr)e^{ik_hr}. \tag{A17}$$